

# Flexible parametrization of generalized parton distributions from deeply virtual Compton scattering observables

Gary R. Goldstein,<sup>1,\*</sup> J. Osvaldo Gonzalez Hernandez,<sup>2,†</sup> and Simonetta Liuti<sup>2,‡</sup>

<sup>1</sup>*Department of Physics and Astronomy, Tufts University, Medford, Massachusetts 02155, USA*

<sup>2</sup>*Department of Physics, University of Virginia, Charlottesville, Virginia 22901, USA*

(Received 16 February 2011; published 5 August 2011)

We present a physically motivated parametrization of the chiral-even generalized parton distributions in the nonsinglet sector obtained from a global analysis using a set of available experimental data. Our analysis is valid in the kinematical region of intermediate Bjorken  $x$  and for  $Q^2$  in the multi-GeV region which is accessible at present and currently planned facilities. Relevant data included in our fit are from the nucleon elastic form factor measurements and from deep inelastic scattering experiments. Additional information provided by lattice calculations of the higher moments of generalized parton distributions is also considered. Recently extracted observables from deeply virtual Compton scattering on the nucleon are reproduced by our fit.

DOI: 10.1103/PhysRevD.84.034007

PACS numbers: 13.60.Hb, 13.40.Gp, 24.85.+p

## I. INTRODUCTION

High-energy exclusive leptonproduction processes have been drawing increasing attention after a long hiatus since they were first proposed as direct probes of partonic structure. The first exclusive electron proton scattering experiments were conducted at both DESY (H1, ZEUS, and HERMES) and Jefferson Lab. A new forthcoming dedicated set of experiments are currently being performed and planned at both Jefferson Lab [1] and CERN (COMPASS) [2]. The possibility of using neutrino beams to study hard exclusive reactions also concretely exists within, e.g., the Minerva experiment at Fermilab [3].

The interest in deeply virtual exclusive processes originates from the realization first discussed in Refs. [4–6] that QCD factorization theorems similar to the inclusive deep inelastic scattering (DIS) case can be proven. Collinear factorization theorems have, in fact, so far been established for deeply virtual Compton scattering (DVCS), involving initially transverse photons, and for deeply virtual meson production (DVMP), with initial longitudinal photons [7]. New developments in QCD factorization are also rapidly evolving [8]. The leading-order diagrams describing the amplitude for the scattering process are shown in Fig. 1. A phenomenology ensues similar to the one extensively developed for inclusive scattering, an important difference being that exclusive reactions provide us with additional kinematical dependence on the momentum transfer squared between the initial and final proton,  $t$ , and on its light cone (LC) component,  $\zeta$ . The new  $t$ -channel variables allow us to pin down, in principle, the dependence of the parton distributions on spatial d.o.f. through Fourier transforms of the generalized parton distributions (GPDs) [9].

The latter enter the description of the soft matrix elements for DVCS, DVMP, and related processes. The kinematical variables external to the partonic loop in Fig. 1(a) are the initial photon's virtuality,  $Q^2$ , the skewness,  $\zeta = (\Delta q)/(Pq) \simeq Q^2/2(Pq) \equiv x_{Bj}$ ,  $t = \Delta^2$ , with  $\Delta = P - P'$ ,  $P$  ( $P'$ ) being the initial (final) photon momentum.  $(\zeta, t, Q^2)$  define a set of independent invariants. In the factorized approach, one defines also internal loop variables,  $X = (kq)/(Pq)$ —the parton's momentum fraction—and  $k_T$ —the intrinsic transverse momentum.

At high momentum transfer, the amplitude for DVCS can be written schematically as

$$T^{\mu\nu}(\zeta, t, Q^2) = \frac{1}{2} g_T^{\mu\nu} \bar{U}(P') \not{U}(P) \sum_q e_q^2 \mathcal{H}_q(\zeta, t, Q^2), \quad (1)$$

where we considered for ease of presentation only the GPD  $H$  (detailed expressions will be given in what follows). The analog of the Compton form factor (CFF) with one virtual photon is

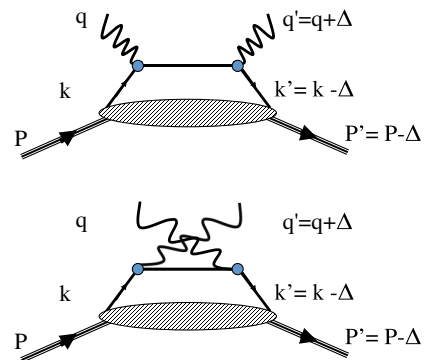


FIG. 1 (color online). Leading-order amplitude for the DVCS process,  $\gamma^* + P \rightarrow \gamma + P'$ .

\*gary.goldstein@tufts.edu

†jog4m@virginia.edu

‡sl4y@virginia.edu

$$\mathcal{H}_q(\zeta, t, Q^2) = \int_{-1+\zeta}^{+1} dX H_q(X, \zeta, t, Q^2) \left( \frac{1}{X-\zeta+i\epsilon} + \frac{1}{X-i\epsilon} \right). \quad (2)$$

One has, therefore, that both the imaginary and real parts of the amplitude, namely,

$$\text{Im}\mathcal{H}_q(\zeta, t) = \pi[H_q(\zeta, \zeta, t) - H_q(0, \zeta, t)], \quad (3a)$$

$$\text{Re}\mathcal{H}_q(\zeta, t) = P.V. \int_{-1}^1 dX H_q(X, \zeta, t) \left( \frac{1}{X-\zeta} + \frac{1}{X} \right), \quad (3b)$$

enter the description of the DVCS reaction. Information on the partonic distributions, which is contained  $H_q(X, \zeta, t)$ , needs to be extracted from these observables. This is an important difference with DIS where, because of the optical theorem, the cross section, by definition, measures the imaginary part of the forward amplitude. The DIS cross section is, therefore, directly proportional to linear combinations of the soft matrix elements or parton distribution functions (PDFs) convoluted with appropriate Wilson coefficient functions. On the contrary, in DVCS, DVMP, and related processes, one needs to disentangle both the real and imaginary contributions of the CFFs defined in Eqs. (3a) and (3b) [10].

It was recently suggested to use dispersion relations in order to relate the real and imaginary parts of CFFs. However, as we noted in [11], dispersion relations do not apply straightforwardly because of the appearance of  $t$ -dependent physical thresholds. As a result, we reiterate that both the real and imaginary parts need to be extracted separately from experiment, at variance with the simplification suggested, e.g., in Refs. [12,13].

On one hand, the type of information we wish to obtain from high-energy exclusive experiments is a sufficiently large range of GPD values in  $(\zeta, t, Q^2)$  that would enable us to reconstruct the partonic spatial distributions of the nucleon from a Fourier transformation in  $\Delta_\perp$ . This would allow us both to explore the holographic principle for the nucleon and to connect to transverse momentum distributions. On the other hand, it is important to have access to the spin flip GPD,  $E$ , which is essential for determining the orbital angular momentum contribution to the spin sum rule.

The question of whether the various GPDs can be extracted reliably from current experiments has been raised, given the complications inherent both in their convolution form and in their complex multivariable analysis (see, e.g., [14,15]). A pragmatic response was given in [16,17] where an assessment was made of which GPDs can be extracted using the present body of data from Jefferson Lab and Hermes. In particular, it was concluded that the only CFFs that are presently constrained by experiments are  $\text{Re}\mathcal{H}$  and  $\text{Im}\mathcal{H}$ , with rather large errors, up to 30%. A global fit using the dual model of Ref. [14], valid mostly at low Bjorken  $x$ , was also conducted in [15]. However, these approaches raise many concerns. In particular, can the

“dual model” used in the fits accommodate all of the data with the given number of parameters? The problem is critical, in particular, for both higher  $\zeta$  values and for the real CFFs. Furthermore, the analysis of [17] does obtain model-independent extractions of CFFs at the expense of not allowing for extrapolations to kinematical domains beyond the very sparse data sets.

The goal of our fit is to extract the GPDs from a variety of experiments under the following basic assumptions:

- (i) QCD factorization is working, namely, the soft and hard parts are separated, as shown in Fig. 1;
- (ii) and the GPDs contributing to DVCS are evaluated at the lowest order in QCD.

This situation is somewhat similar to the extraction of PDFs from structure functions at next-to-leading order, where the PDFs are convoluted with the next-to-leading-order Wilson coefficient functions. The convolution is neither a substantial or conceptual obstacle, so long as one is providing an appropriate initial functional shape. The strategy we propose here provides a parametric form of the chiral-even GPDs— $H$ ,  $E$ ,  $\tilde{H}$ , and  $\tilde{E}$ —that is valid in the multi-GeV, intermediate  $x_{Bj}$  region accessible at Jefferson Lab and COMPASS.

We suggest the idea that, for extracting GPDs from experiment, a *progressive/recursive fit* should be used, rather than a global fit. In our fitting procedure, constraints are applied sequentially, the final result being updated upon including each new constraint. In a nutshell, in a first step, we provide a flexible form that includes all constraints from inclusive data—DIS structure functions and elastic electro-weak form factors. We subsequently evaluate the impact of presently available DVCS data from both Jefferson Lab and Hermes. The data set used in our analysis is consistent with the one from Ref. [16]. The parametric form is based on a “Regge improved” diquark model that, because of its similarities and possible connections with the dual model [18], we call the *hybrid model*.

Our approach, however, makes two important distinctions: i) we attack the GPD parametrization issue from the bottom-up perspective. We adopt a flexible parametrization that is consistent with theoretical constraints imposed numerically and let the experimental data guide the shape of the parametrization as closely as possible. In this procedure, experimental evidence is used to constrain the various theoretical aspects of the GPDs’ behavior, eventually giving rise to a complete model; ii) our model differs from some of the lore on the partonic interpretation of GPDs in the Efremov-Radyushkin-Brodsky-Lepage (ERBL) region. In Ref. [19], we, in fact, pointed out that the ERBL region, or the region with  $X < \zeta$ , cannot be described in terms of a quark antiquark pair emerging from the nucleon because of the presence of semidisconnected, unphysical diagrams associated to this configuration (Fig. 2). While casting a doubt on any partonic picture in the ERBL region, we also suggested that multiparton

distributions may restore the connectedness and, consequently, the partonic interpretation of the DVCS graphs. In this paper, we, therefore, adopted, as a practical scheme, the hybrid model in the Dokshitzer-Gribov-Lipatov-Altarelli-Paris (DGLAP) ( $X > \zeta$ ) region and a minimal model that is consistent with the properties of continuity at  $X = \zeta$ , polynomiality, and crossing symmetry for the ERL region (see, e.g., [20] for a review).

Details on the model are given in Sec. II. The new fitting procedure is described in Sec. III. In Sec. IV, we discuss the implementation of world DVCS data. Finally, in Sec. V, we draw our conclusions and outline future work.

## II. COVARIANT FORMULATION AND SYMMETRIES

We begin by describing the connection between the Dirac basis formulation of the correlation function and the helicity amplitude formalism in DVCS. Some of this formalism was outlined in Refs. [20,21]. We, however, present here the formal details that will be important for the extraction of observables in Sec. IV.

### A. Formalism

The factorization theorem for hard scattering processes allows us to separate the hard scattering between the elementary constituents, which is calculated using perturbative QCD, from the soft hadronic matrix element,  $\mathcal{M}$ , as

$$T^{\mu\nu} = -i \int \frac{d^4k}{(2\pi)^4} \text{Tr} \left[ \left( \frac{\gamma^\mu i(\not{k} + \not{q}) \gamma^\nu}{(k+q)^2 + i\epsilon} + \frac{\gamma^\nu i(\not{k} - \not{X} - \not{q}) \gamma^\mu}{(k-\Delta-q)^2 + i\epsilon} \right) \mathcal{M}(k, P, \Delta) \right]. \quad (4)$$

$\mathcal{M}(k, P, \Delta)$  is the off-forward correlation function

$$\mathcal{M}_{ij}^{\Lambda\Lambda'}(k, P, \Delta) = \int d^4y e^{iky} \langle P', \Lambda' | \bar{\psi}_j(0) \psi_i(y) | P, \Lambda \rangle, \quad (5)$$

where we have written out explicitly both the Dirac indices  $i, j$  and the target's spins  $\Lambda, \Lambda'$ . By projecting out the dominant contribution in the Bjorken limit ( $Q^2 \rightarrow \infty$ ,  $x_{Bj} = Q^2/2M\nu \approx \zeta$ , and  $t$  fixed), which corresponds to transverse virtual photon polarization, one obtains

$$T^{\mu\nu} = \frac{1}{2} g_T^{\mu\nu} \mathcal{F}_S^{\Lambda\Lambda'} + \frac{i}{2} \epsilon_T^{\mu\nu} \mathcal{F}_A^{\Lambda\Lambda'}, \quad (6)$$

where  $g_T^{\mu\nu} = g^{\mu\nu} - p^\mu n^\nu - p^\nu n^\mu$ ,  $\epsilon_T^{\mu\nu} = \epsilon_{\alpha\beta\sigma\rho} g_T^{\alpha\mu} g_T^{\beta\nu} n^\rho p^\sigma \equiv \epsilon^{-+\mu\nu}$ ,  $p$  and  $n$  being unit light cone vectors. The labels  $S$  and  $A$  refer to the symmetric and antisymmetric components of the hadronic tensor, with respect to  $\mu \leftrightarrow \nu$ , that will enter the unpolarized and longitudinally polarized scattering, respectively, as will be clarified in what follows.

A possible kinematical choice is the one where the struck quark's LC longitudinal component is  $k^+ = XP^+$

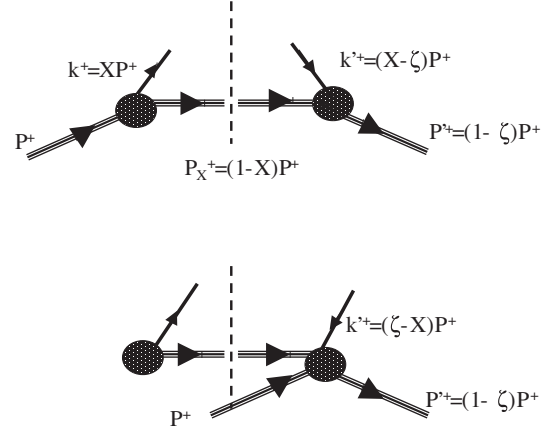


FIG. 2. Left: amplitude for DVCS at leading order in  $Q^2$ . The light cone components of the momenta for the active quarks and nucleons are explicitly written. Right: Time-ordered diagrams for DVCS: (a) dominant contribution in the  $X > \zeta$  region; (b) a  $q\bar{q}$  pair is first produced from the nucleon and subsequently interacts with the photons. This process dominates the  $X < \zeta$  region. The crossed terms where two of the particles in the same class are switched are not shown in the figure.

and the momentum transfer,  $\Delta_\mu$ , is decomposed into a LC longitudinal component,  $\Delta^+ = \zeta P^+$ , and a transverse component,  $\Delta_\perp$ , such that the invariant  $t = \Delta^2$  reads  $t = -\zeta^2 M^2 / (1 - \zeta) - \frac{\Delta_\perp^2}{1 - \zeta}$ .<sup>1</sup> Using these variables, one can perform an integration over the quark loop momentum, namely,  $d^4k \equiv dk^+ dk^- d^2k_\perp \equiv P^+ dX dk^- d^2k_\perp$ , obtaining the following expressions for the CFFs:

$$\mathcal{F}_{\Lambda, \Lambda'}^S(\zeta, t) = \int_{-1+\zeta}^1 dX \left( \frac{1}{X - \zeta + i\epsilon} + \frac{1}{X - i\epsilon} \right) F_{\Lambda, \Lambda'}^S(X, \zeta, t), \quad (7)$$

$$\mathcal{F}_{\Lambda, \Lambda'}^A(\zeta, t) = \int_{-1+\zeta}^1 dX \left( -\frac{1}{X - \zeta + i\epsilon} + \frac{1}{X - i\epsilon} \right) F_{\Lambda, \Lambda'}^A(X, \zeta, t), \quad (8)$$

where

$$F_{\Lambda, \Lambda'}^S(X, \zeta, t) = \frac{1}{2\bar{P}^+} \left[ \bar{U}(P', \Lambda') \left( \gamma^+ H(X, \zeta, t) + \frac{i\sigma^{+\mu}(-\Delta_\mu)}{2M} E(X, \zeta, t) \right) U(P, \Lambda) \right], \quad (9)$$

$$F_{\Lambda, \Lambda'}^A(X, \zeta, t) = \frac{1}{2\bar{P}^+} \left[ \bar{U}(P', \Lambda') \left( \gamma^+ \gamma_5 \tilde{H}(X, \zeta, t) + \gamma_5 \frac{-\Delta^+}{2M} \tilde{E}(X, \zeta, t) \right) U(P, \Lambda) \right]. \quad (10)$$

The GPDs— $H$ ,  $E$ ,  $\tilde{H}$ , and  $\tilde{E}$ —introduced in the equations include the integration over  $dk^- d^2k_\perp$ ;  $\bar{P}^+ = (P^+ + P'^+)/2$ ,

<sup>1</sup>The formal difference between the so-called symmetric and asymmetric notations is explained, e.g., in Ref. [20].

and we did not write explicitly, for simplicity, both the label for the different quark components and the dependence on the scale of the process,  $Q^2$ .

Equations (9) and (10) define the basic Dirac structure for the chiral-even sector at leading order in  $1/Q$ . The connection with the helicity formalism is made by introducing the helicity amplitudes for DVCS,

$$f_{\Lambda_\gamma, \Lambda; \Lambda'_\gamma, \Lambda'} = \epsilon_\mu^{\Lambda_\gamma} T_{\Lambda\Lambda'}^{\mu\nu} \epsilon_\nu^{*\Lambda'_\gamma}, \quad (11)$$

where  $\epsilon_\mu^\Lambda$  are the photon polarization vectors,  $(\Lambda_\gamma, \Lambda)$  refer to the initial (virtual) photon and proton helicities, and  $(\Lambda'_\gamma, \Lambda')$  to the final ones. The following decomposition of  $f_{\Lambda_\gamma, \Lambda; \Lambda'_\gamma, \Lambda'}$  [21] can be made as

$$f_{\Lambda_\gamma, \Lambda; \Lambda'_\gamma, \Lambda'} = \sum_{\lambda, \lambda'} g_{\lambda, \lambda'}^{\Lambda_\gamma, \Lambda'_\gamma}(X, \zeta, t; Q^2) \otimes A_{\Lambda', \lambda'; \Lambda, \lambda}(X, \zeta, t), \quad (12)$$

where  $g_{\lambda, \lambda'}^{\Lambda_\gamma, \Lambda'_\gamma}$  describes the partonic subprocess  $\gamma^* + q \rightarrow \gamma + q$ , i.e., the scattering of a transverse virtual photon from a quark with polarization  $\lambda$ ;  $A_{\Lambda', \lambda'; \Lambda, \lambda}$  is the quark-proton helicity amplitude, and the convolution integral is given by  $\otimes \rightarrow \int_{-\zeta+1}^1 dX$ . In the Bjorken limit,  $g_{\lambda, \lambda'}^{\Lambda_\gamma, \Lambda'_\gamma}$  reads

$$g_{\lambda, \lambda'}^{\Lambda_\gamma, \Lambda'_\gamma}(X, \zeta) = [\bar{u}(k', \lambda') \gamma^\mu \gamma^+ \gamma^\nu u(k, \lambda)] \times \left( \frac{\epsilon_\mu^{\Lambda_\gamma} \epsilon_\nu^{*\Lambda'_\gamma}}{\hat{s} - i\epsilon} + \frac{\epsilon_\mu^{*\Lambda'_\gamma} \epsilon_\nu^{\Lambda_\gamma}}{\hat{u} - i\epsilon} \right) q^-, \quad (13)$$

with  $\hat{s} = (k + q)^2 \approx Q^2(X - \zeta)/\zeta$ ,  $\hat{u} = (k' - q)^2 \approx Q^2 X/\zeta$ , and  $q^- \approx (Pq)/P^+ = Q^2/(2\zeta P^+)$ .

For DVCS, one can consider either the sum over the transverse helicities of the initial photon, i.e., we take it as unpolarized, or the difference of the helicities, in which case the transverse photon is polarized. The outgoing photon is on-shell, and thus purely transverse or helicity  $\pm 1$ . So, the leading incoming virtual photon will have the same helicity in the collinear limit. Only  $g_{+,+}^{+,+}$  ( $= g_{-, -}^{-, -}$  via Parity conservation) for the direct  $\hat{s}$  pole term or  $g_{+,+}^{-, -}$  ( $= g_{-, -}^{+, +}$ ) for the crossed  $\hat{u}$  pole term will survive. For either allowed combination,  $g_{++}^S = g_{++}^{+,+} + g_{+-}^{-, -}$  and  $g_{+-}^A = g_{++}^{+,+} - g_{+-}^{-, -}$ ,

$$g_{++}^{+,+} \pm g_{+-}^{-, -} = \sqrt{X(X-\zeta)} \left( \frac{1}{X-\zeta+i\epsilon} \pm \frac{1}{X-i\epsilon} \right), \quad (14)$$

where we use the  $S/A$  labels for the sum/difference between the positive and negative polarized photons for the overall process representing the sum/difference between the quark states' helicities that arises as the quarks emerge from the nucleons.

The quark helicity or chirality is conserved in this hard subprocess for DVCS. Hence, the  $A_{\Lambda', \lambda'; \Lambda, \lambda}$  will be chiral-even. Equation (14) is the Wilson coefficient from Ref. [5] times a kinematical factor that will cancel out when multiplied by the soft part, as described below.

The convolution in Eq. (12) yields the following decomposition of the transverse photon helicity amplitudes:

$$f_{++}^S = f_{+,+,+} + f_{-,-,-} = g_{++}^S \otimes (A_{+,+,+} + A_{-,-,-}), \quad (15a)$$

$$f_{++}^A = f_{+,+,+} - f_{-,-,-} = g_{++}^A \otimes (A_{+,+,+} - A_{-,-,-}), \quad (15b)$$

$$f_{+-}^S = f_{+,+,-} + f_{-,-,+} = g_{+-}^S \otimes (A_{-,+,+} + A_{+,-,-}), \quad (15c)$$

$$f_{+-}^A = f_{+,+,-} - f_{-,-,+} = g_{+-}^A \otimes (A_{-,+,+} - A_{+,-,-}), \quad (15d)$$

where, because of parity conservation,  $A_{-,-,-} = A_{+,+,+}$ ,  $A_{-,+,-} = A_{+,-,+}$ ,  $A_{-,-,+} = -A_{+,+,-}^*$ , and  $A_{+,-,-} = -A_{-,-,+}^*$ .

By calculating explicitly the matrix elements in Eqs. (7) and (8), using the relations below,

$$\frac{1}{2\bar{P}^+} \bar{U}(P', \Lambda') \gamma^+ U(P, \Lambda) = \frac{\sqrt{1-\zeta}}{1-\zeta/2} \delta_{\Lambda, \Lambda'}, \quad (16a)$$

$$\frac{\sqrt{1-\zeta}}{2\bar{P}^+} \bar{U}(P', \Lambda') \frac{i\sigma^{+\mu}}{2M} \Delta_\mu U(P, \Lambda) = \frac{-\zeta^2/4}{(1-\zeta/2)} \delta_{\Lambda, \Lambda'} + \frac{-\Lambda\Delta_1 - i\Delta_2}{2M} \delta_{\Lambda, -\Lambda'}, \quad (16b)$$

$$\frac{1}{2\bar{P}^+} \bar{U}(P', \Lambda') \gamma^+ \gamma_5 U(P, \Lambda) = \Lambda \frac{\sqrt{1-\zeta}}{1-\zeta/2} \delta_{\Lambda, \Lambda'}, \quad (16c)$$

$$\frac{\sqrt{1-\zeta}}{2\bar{P}^+} \bar{U}(P', \Lambda') \gamma_5 \frac{\Delta^+}{2M} U(P, \Lambda) = \frac{\zeta}{2(1-\zeta/2)} \left( \Lambda\zeta \delta_{\Lambda, \Lambda'} + \frac{\Delta_1 - i\Lambda\Delta_2}{M} \delta_{\Lambda, -\Lambda'} \right), \quad (16d)$$

one obtains the various helicity amplitudes written in terms of the following combinations of CFFs for the symmetric part,

$$f_{+,+}^S = \frac{\sqrt{1-\zeta}}{1-\zeta/2} \mathcal{H} + \frac{-\zeta^2/4}{(1-\zeta/2)\sqrt{1-\zeta}} \mathcal{E}, \quad (17a)$$

$$f_{+,-}^S = \frac{1}{\sqrt{1-\zeta}} \frac{1}{1-\zeta/2} \frac{\Delta_1 + i\Delta_2}{2M} \mathcal{E} \quad (17b)$$

and

$$f_{+,+}^A = \frac{\sqrt{1-\zeta}}{1-\zeta/2} \tilde{\mathcal{H}} + \frac{-\zeta^2/4}{(1-\zeta/2)\sqrt{1-\zeta}} \tilde{\mathcal{E}}, \quad (18a)$$

$$f_{+,-}^A = \frac{\zeta}{\sqrt{1-\zeta}} \frac{1}{1-\zeta/2} \frac{\Delta_1 + i\Delta_2}{2M} \tilde{\mathcal{E}} \quad (18b)$$

for the antisymmetric component.

A similar formalism was presented in [20], where, however, the helicity amplitudes were identified with the combinations

$$f_{++}^S + f_{++}^A, f_{++}^S - f_{++}^A, f_{+-}^S + f_{+-}^A, f_{+-}^S - f_{+-}^A.$$

Here, differently from [20], we distinguish between the two possible circular polarizations for the transverse virtual photon that generate the  $S$  and  $A$  components. Such components are written out explicitly throughout this paper.

## B. The hybrid model

We evaluate the quark-parton helicity amplitudes in Eq. (12) using a covariant model. The simplest realization of the covariant formalism is the quark-diquark model in which the initial proton dissociates into a quark and a recoiling fixed mass system with quantum numbers of a diquark (Fig. 1). The covariant model can be made more general by letting the mass of the diquark system vary according to a spectral distribution. Extending the diquark mass value generalization corresponds to ‘‘Reggeizing’’ the covariant model, since the spectral distribution can then reproduce the Regge behavior, which is necessary to describe the low  $X$  behavior (a likewise scenario was considered in the pioneering work of Ref. [22]). Keeping this in mind, in this paper, we will include a Regge term multiplicatively, as shown later on. Because we introduce similarities or open possible connections with the dual model of Ref. [18], we denote this model of GPDs the *hybrid model*.

For reasons explained in the Introduction, we adopt the diquark model only for the DGLAP region, where  $X \geq \zeta$ . The DGLAP region can be considered a direct extension of the parton model, where the struck quark with initial longitudinal momentum fraction  $X$  is reinserted in the proton target after reducing its momentum fraction to  $X - \zeta$ ,  $\zeta$  being the fraction transferred in the exclusive reaction. In the DGLAP region, the initial and final quarks are both off-shell, while the diquark intermediate state is on mass shell. The soft part,  $A_{\Lambda',\Lambda;\Lambda,\lambda}$ , is described in terms of GPDs.  $A$  is given by an integral over the  $k^-$  and  $k_\perp$  variables (see Appendix B for detailed expressions). In the DGLAP region, the three soft propagators corresponding to the quark that is emitted  $(k^2 - m^2)^{-1}$ , the quark that is reabsorbed  $(k'^2 - m^2)^{-1}$ , and to the intermediate diquark system  $(P_X^2 - M_X^2)^{-1}$  have poles that lie, respectively, on the negative imaginary  $k^-$  axis ( $k, k'$ ) and on the positive axis ( $P_X$ ). Therefore, one closes the integration contour on

the positive side, and the diquark is on its mass shell (see also [23]).

As for the spin structure of the propagators, we have adopted the same scheme as in Refs. [24,25], where we considered both the  $S = 0$  (scalar) and  $S = 1$  (axial-vector) configurations for the diquark. This allows one to obtain distinct predictions for the  $u$  and  $d$  quarks. However, we assume a similar form for the scalar and axial-vector couplings (scalarlike) and we distinguish their different contributions by varying their respective mass parameters in the calculations. This assumption is in line with previous estimates [24–26], where it was advocated that the full account of the axial-vector coupling does not sensibly improve the shape of parametrizations, while considerably increasing the algebraic complexity of the various structures (see, e.g., [27]). We define  $\Gamma$  as the scalar coupling at the proton-quark-diquark vertex

$$\Gamma = g_s \frac{k^2 - m^2}{(k^2 - M_\Lambda^2)^2},$$

$g_s$  being a constant.<sup>2</sup> The quark-proton helicity amplitudes are defined as

$$A_{\Lambda',\Lambda;\Lambda,\lambda} = \int d^2k_\perp \phi_{\Lambda',\Lambda}^*(k', P') \phi_{\Lambda,\lambda}(k, P), \quad (19)$$

with

$$\begin{aligned} \phi_{\Lambda,\lambda}(k, P) &= \Gamma(k) \frac{\bar{u}(k, \lambda) U(P, \Lambda)}{k^2 - m^2}, \\ \phi_{\Lambda',\lambda'}^*(k', P') &= \Gamma(k') \frac{\bar{U}(P', \Lambda') u(k', \lambda')}{k'^2 - m^2} \end{aligned}$$

defining the helicity structures at each soft vertex.  $\phi$  is real,  $\phi_{\Lambda\lambda} = \phi_{\Lambda\lambda}^*$ , for  $\Lambda = \lambda$ , whereas  $\phi_{+-} = -\phi_{-+}^*$ . We list the separate structures appearing in Eqs. (19):

$$A_{++++} = \int d^2k_\perp \phi_{++}^*(k', P') \phi_{++}(k, P), \quad (20a)$$

$$A_{+-+-} = \int d^2k_\perp \phi_{+-}^*(k', P') \phi_{+-}(k, P), \quad (20b)$$

$$A_{-+ ++} = \int d^2k_\perp \phi_{-+}^*(k', P') \phi_{++}(k, P), \quad (20c)$$

$$A_{++-+} = \int d^2k_\perp \phi_{++}^*(k', P') \phi_{-+}(k, P), \quad (20d)$$

where

<sup>2</sup>The choice of this vertex function is motivated by phenomenological reasons—it allows for an easier fit of the form factors—and also because it agrees with predictions within the Schwinger-Dyson formalism. See discussions in [24,25] and in [23].

$$\phi_{++}(k, P) = \frac{1}{\sqrt{X}}(m + MX) \frac{\Gamma(k)}{k^2 - m^2}, \quad (21a)$$

$$\phi_{++}(k', P') = \sqrt{\frac{1-\zeta}{X-\zeta}} \left( m + M \frac{X-\zeta}{1-\zeta} \right) \frac{\Gamma(k')}{k'^2 - m^2}, \quad (21b)$$

$$\phi_{+-}(k, P) = \frac{1}{\sqrt{X}}(k_1 - ik_2) \frac{\Gamma(k)}{k^2 - m^2}, \quad (21c)$$

$$\phi_{+-}(k', P') = \sqrt{\frac{1-\zeta}{X-\zeta}} (\tilde{k}_1 - i\tilde{k}_2) \frac{\Gamma(k')}{k'^2 - m^2}, \quad (21d)$$

with  $\tilde{k}_i = k_i - (1-X)/(1-\zeta)\Delta_i$  ( $i = 1, 2$ ).

Finally, the denominators are evaluated with the diquark mass on shell,

$$k^2 - m^2 = XM^2 - \frac{X}{1-X}M_X^2 - m^2 - \frac{k_\perp^2}{1-X}, \quad (22a)$$

$$k'^2 - m^2 = \frac{X-\zeta}{1-\zeta}M^2 - \frac{X-\zeta}{1-X}M_X^2 - m^2 - \frac{1-\zeta}{1-X} \left( \mathbf{k}_\perp - \frac{1-X}{1-\zeta} \mathbf{\Delta}_\perp \right)^2. \quad (22b)$$

To extract the GPDs, we calculate the convolutions in Eqs. (15) using the expressions for the  $g$  and  $A$  functions evaluated above. We obtain

$$\begin{aligned} & \mathcal{N} \frac{\sqrt{1-\zeta}}{1-X} \int d^2k_\perp \frac{[(m+MX)(m+M\frac{X-\zeta}{1-\zeta}) + \mathbf{k}_\perp \cdot \tilde{\mathbf{k}}_\perp]}{(k^2 - M_\Lambda^2)^2(k'^2 - M_\Lambda^2)^2} \\ &= \frac{\sqrt{1-\zeta}}{1-\zeta/2} H + \frac{-\zeta^2/4}{(1-\zeta/2)\sqrt{1-\zeta}} E, \end{aligned} \quad (23)$$

$$\begin{aligned} & \mathcal{N} \frac{\sqrt{1-\zeta}}{1-X} \int d^2k_\perp \\ & \times \frac{[(m+MX)(\tilde{k}_1 + i\tilde{k}_2) - (m+M\frac{X-\zeta}{1-\zeta})(k_1 + ik_2)]}{(k^2 - M_\Lambda^2)^2(k'^2 - M_\Lambda^2)^2} \\ &= \frac{1}{\sqrt{1-\zeta}(1-\zeta/2)} \frac{\Delta_1 + i\Delta_2}{2M} E, \end{aligned} \quad (24)$$

$$\begin{aligned} & \mathcal{N} \frac{\sqrt{1-\zeta}}{1-X} \int d^2k_\perp \frac{[(m+MX)(m+M\frac{X-\zeta}{1-\zeta}) - \mathbf{k}_\perp \cdot \tilde{\mathbf{k}}_\perp]}{(k^2 - M_\Lambda^2)^2(k'^2 - M_\Lambda^2)^2} \\ &= \frac{\sqrt{1-\zeta}}{1-\zeta/2} \tilde{H} + \frac{-\zeta^2/4}{(1-\zeta/2)\sqrt{1-\zeta}} \tilde{E}, \end{aligned} \quad (25)$$

$$\begin{aligned} & \mathcal{N} \frac{\sqrt{1-\zeta}}{1-X} \int d^2k_\perp \\ & \times \frac{[(m+MX)(\tilde{k}_1 + i\tilde{k}_2) + (m+M\frac{X-\zeta}{1-\zeta})(k_1 + ik_2)]}{(k^2 - M_\Lambda^2)^2(k'^2 - M_\Lambda^2)^2} \\ &= \frac{\zeta/2}{\sqrt{1-\zeta}(1-\zeta/2)} \frac{\Delta_1 + i\Delta_2}{2M} \tilde{E}, \end{aligned} \quad (26)$$

from which the following forms for  $H$ ,  $E$ ,  $\tilde{H}$ , and  $\tilde{E}$  can be derived:

$$\begin{aligned} H &= \mathcal{N} \frac{1-\zeta/2}{1-X} \\ & \times \int d^2k_\perp \frac{[(m+MX)(m+M\frac{X-\zeta}{1-\zeta}) + \mathbf{k}_\perp \cdot \tilde{\mathbf{k}}_\perp]}{(k^2 - M_\Lambda^2)^2(k'^2 - M_\Lambda^2)^2} \\ & + \frac{\zeta^2}{4(1-\zeta)} E, \end{aligned} \quad (27)$$

$$\begin{aligned} E &= \mathcal{N} \frac{1-\zeta/2}{1-X} \int d^2k_\perp \\ & \times \frac{-2M(1-\zeta)[(m+MX)\frac{\tilde{k}_\perp \cdot \Delta_\perp}{\Delta_\perp^2} - (m+M\frac{X-\zeta}{1-\zeta})\frac{k_\perp \cdot \Delta_\perp}{\Delta_\perp^2}]}{(k^2 - M_\Lambda^2)^2(k'^2 - M_\Lambda^2)^2}, \end{aligned} \quad (28)$$

$$\begin{aligned} \tilde{H} &= \mathcal{N} \frac{1-\zeta/2}{1-X} \\ & \times \int d^2k_\perp \frac{[(m+MX)(m+M\frac{X-\zeta}{1-\zeta}) - \mathbf{k}_\perp \cdot \tilde{\mathbf{k}}_\perp]}{(k^2 - M_\Lambda^2)^2(k'^2 - M_\Lambda^2)^2} \\ & + \frac{\zeta^2}{4(1-\zeta)} \tilde{E}, \end{aligned} \quad (29)$$

$$\begin{aligned} \tilde{E} &= \mathcal{N} \frac{1-\zeta/2}{1-X} \int d^2k_\perp \\ & \times \frac{-\frac{4M(1-\zeta)}{\zeta} [(m+MX)\frac{\tilde{k}_\perp \cdot \Delta_\perp}{\Delta_\perp^2} + (m+M\frac{X-\zeta}{1-\zeta})\frac{k_\perp \cdot \Delta_\perp}{\Delta_\perp^2}]}{(k^2 - M_\Lambda^2)^2(k'^2 - M_\Lambda^2)^2}, \end{aligned} \quad (30)$$

where  $\mathcal{N}$  is in  $\text{GeV}^4$ . The integrations over  $d^2k_\perp$  yield finite values for the amplitudes in the limits  $\Delta \rightarrow 0$  and  $\zeta \rightarrow 0$  (see Appendix A).

### C. Reggeization

It was noticed in Refs. [24,25] that the low  $X$  behavior of the GPDs in the forward limit necessitates an extra factor of the type  $\approx X^{-\alpha}$  in order to adequately fit current DIS data. We reiterate that, for the off-forward case, this factor is important even at intermediate/large values of  $X$  and  $\zeta$  because the dominant behavior of the GPDs at low  $X$  determines the nucleon form factors. In other words, the lack of such a term hinders a good fit of the form factors.

One way to motivate the inclusion of a Regge term is through a generalization of the diquark picture in which the mass of the diquark,  $M_X^2$ , is not fixed but has a spectral distribution. As first shown in Ref. [22], in a simple covariant model for a PDF, choosing a spectral distribution of the form  $\rho_R(M_X^2) \propto M_X^{2\alpha(0)}$  gives rise to the PDF behavior  $x^{-\alpha(0)}$  upon integration over all  $M_X^2$ . A more physical picture of the nucleon might have two contributions,

$$\rho(M_X^2) = \rho_G(M_X^2) + \rho_R(M_X^2), \quad (31)$$

wherein  $\rho_G$  is sharply peaked at a fixed value of the diquark mass  $M_X^2 = \bar{M}_X^2$  and it yields the usual ‘‘fixed mass’’

diquark model.  $\rho_R$  smoothly extends  $M_X^2$  to large values and, with the Regge power behavior, upon integration over  $M_X^2$ , will yield a Regge-type behavior largely dictated by the shape of the spectral function itself.

We will illustrate this ‘‘Reggeization’’ process by considering the spin-independent GPD  $H(X, 0, 0) = f_1(X)$  as a function of a continuum of diquark masses. Aside from overall constant factors, the exact expression for the forward limit for the mass  $M_X$ , obtained from Eq. (27), is given by

$$H(X, 0, 0) \propto \left[ \frac{2(m_q + XM)^2}{[M_X^2 + \frac{(1-X)}{X}(M_\Lambda^2 - XM^2)]^3} + \frac{X}{[M_X^2 + \frac{(1-X)}{X}(M_\Lambda^2 - XM^2)]^2} \right] \frac{\pi(1-X)^4}{6X^3}. \quad (32)$$

Multiplying this expression with  $\rho_R(M_X^2) \propto M_X^{2\alpha(0)}$  and then integrating over all diquark masses from 0 to  $\infty$  gives the analytic result

$$\int_0^\infty dM_X^2 \rho_R(M_X^2) H(X, 0, 0) \sim X^{-\alpha(0)-1} \quad (33)$$

for  $X \rightarrow 0$ . In practice, we would not integrate from zero mass and we would cut off the integral at the maximum mass allowed by the kinematics. The fixed mass term  $\rho_G(M_X^2)$  would give back the unintegrated expression Eq. (33), which goes to a constant or  $X^0$  as  $X \rightarrow 0$ . A plausible form for the spectral density of the diquark is shown in Fig. 3.

Our main conclusion is that we can generate the Regge behavior and still be consistent with the diquark model. This is further borne out by recalling that, in a dual model for the virtual photon-hadron scattering, there will be Regge behavior in the high  $s$  region multiplying pole terms for the intermediate states, which here would be diquarks. This suggests that, for the exclusive processes, particularly DVCS, the GPDs will have the factorized form of a Regge

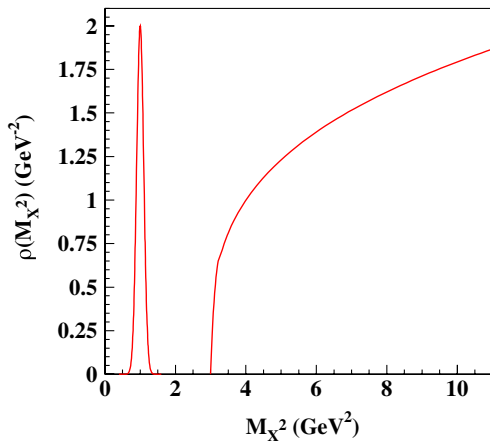


FIG. 3 (color online). A plausible diquark mass distribution, the spectral density with Regge behavior  $M_X^{2\alpha(0)}$  with  $\alpha(0) \approx \frac{1}{3}$ .

function for small  $X$  times a pole at the nearest singularity, the lowest mass diquark, as in Eq. (33). This is the form we take, as we show below.

At this point, this discussion does not consider the  $t$  dependence, although it is plausible to incorporate the Regge trajectory form  $\alpha(t) = \alpha_0 + \alpha't$ , while including the  $t$  dependence of the diquark model. Including the skewness,  $\zeta \neq 0$  is more complicated, because of the distinction between the DGLAP and ERBL regions. While detailed calculations using Eq. (31) will be presented elsewhere, in the present analysis, we adopt a factorized form of the Regge term, which has similar features as the Reggeized diquark model but is more in line with current parametric forms of parton distributions,

$$R = X^{-[\alpha + \alpha'(X)t + \beta(\zeta)t]}. \quad (34)$$

In this form, only the term  $X^{-\alpha}$  can be considered a proper Regge contribution. The term  $\alpha'(X) = \alpha'(1-X)^p$  is constructed so as to guarantee that, upon Fourier transformation in  $\Delta_\perp$ , one obtains finite values for the nucleon radius as  $X \rightarrow 1$  [28]. This prescription is obtained for  $\zeta = 0$  or  $t \equiv -\Delta_\perp^2$  [29]. In order to extend it to  $\zeta \neq 0$ , an additional term in the exponent,  $\beta(\zeta)$ , is introduced. The physical motivation for this term is that it effectively accounts for the shift between the initial and final proton's coordinates that occurs when Fourier transforming GPDs at  $\zeta \neq 0$  [30].

As we will show in Secs. III and IV, two forms of  $\beta$  are suggested by the behavior of the available DVCS data:

$$\beta_I(\zeta) = \beta \frac{\zeta^2}{1 - \zeta}, \quad (35)$$

$$\beta_{II}(\zeta) = \beta \zeta^a. \quad (36)$$

The effect of these terms is to allow for a data driven change in the slope in  $\zeta$  of the GPDs, most likely an increase, with respect to the diquark model predictions. Since most DVCS data, so far, appear as asymmetries given by ratios of different cross section combinations, it is difficult to determine precisely the  $\zeta$  behavior of the CFFs and GPDs. It is, therefore, indispensable in future experimental analyses to provide absolute cross sections, as already done for the set of data provided by Hall A. Introducing directly DVCS data to determine the behavior of our fit is an important step that distinguishes our analysis from other ones in that it helps establishing the main trends of the multivariable-dependent data. The treatment of multivariable dependence characterizes analyses aimed at extracting GPDs from data. What we suggest here is a bottom-up approach where experimental evidence is used to constrain the various theoretical aspects of the GPDs' behavior, eventually giving rise to a complete model.

#### D. Crossing symmetries

GPDs observe precise crossing symmetry relations. In order to discuss these symmetry properties, we first

introduce the so-called ‘‘symmetric system’’ of variables  $\{x, \xi\}$ , where

$$x = \frac{k^+ + k'^+}{P^+ + P'^+} = \frac{X - \zeta/2}{1 - \zeta/2}, \quad \xi = \frac{2\Delta^+}{P^+ + P'^+} = \frac{\zeta}{2 - \zeta}.$$

We also introduce the quark labels for all four chiral-even GPDs,  $F_q \equiv \{H_q, E_q, \tilde{H}_q, \tilde{E}_q\}$ . By analogy with DIS, we define  $F_q(x, \xi)$  in the interval  $-1 \leq x \leq 1$ , with the following identification of antiquarks:

$$F_{\bar{q}}(x, \xi) = -F_q(x, \xi), \quad x < 0. \quad (37)$$

From this expression, one defines

$$F_q^- = F_q(x, \xi) - F_{\bar{q}}(x, \xi), \quad (38)$$

$$F_q^+ = F_q(x, \xi) + F_{\bar{q}}(x, \xi), \quad (39)$$

where  $F_q^-$  is identified with the flavor nonsinglet valence quark distributions, and  $\sum_q F_q^+$  with the flavor singlet sea quark distributions.  $F_q^-$  and  $F_q^+$  obey the symmetry relations

$$F_q^-(x, \xi) = F_q^-(-x, \xi), \quad (40)$$

$$F_q^+(x, \xi) = -F_q^+(-x, \xi). \quad (41)$$

In DIS, the commonly adopted Kuti-Weisskopf model ensues [31], by which all distributions are evaluated at positive  $x$ .

In the off-forward case, crossing symmetries are important for the evaluation of the CFFs defined in Eq. (2). The Wilson coefficient function, in fact, also obeys crossing symmetry relations,

$$C^\pm(x, \xi) = \frac{1}{x - \xi + i\epsilon} \pm \frac{1}{x + \xi - i\epsilon}, \quad (42)$$

so that

$$\mathcal{H}_q = \int_0^1 dx C^+(x, \xi) H_q^+(x, \xi, t), \quad (43)$$

$$\tilde{\mathcal{H}}_q = \int_0^1 dx C^-(x, \xi) \tilde{H}_q^-(x, \xi, t), \quad (44)$$

and similar relations hold for  $E_q$  and  $\tilde{E}_q$ . In the nonsymmetric system of variables adopted throughout this paper, the axis of symmetry is shifted to  $X = \zeta/2$ . Moreover,  $x \in [-1, 1] \Rightarrow X \in [-1 + \zeta, 1]$ , and  $x = -\xi \Rightarrow X = 0$ ,  $x = \xi \Rightarrow X = \zeta$ .

As explained in the Introduction, the validity of a simple handbag-based partonic interpretation of DVCS in the ERBL region has been recently questioned. The safest choice for a parametrization in the ERBL region is, therefore, to adopt a ‘‘minimal’’ model that accounts for crossing symmetry properties, continuity at the crossover points ( $X = 0$  and  $X = \zeta$ ), and polynomiality. A possible form is obtained by parametrizing the crossing symmetric and antisymmetric contributions, respectively, as follows:

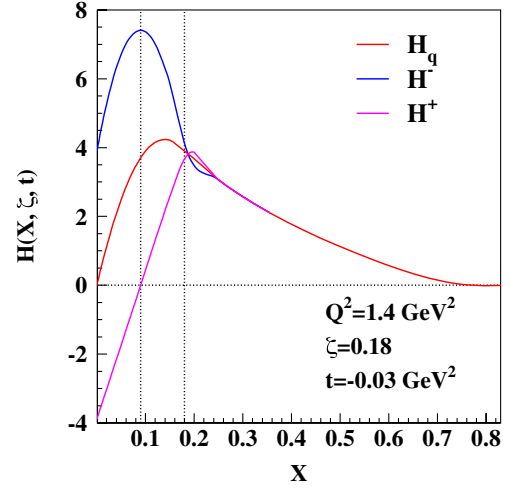


FIG. 4 (color online). Crossing symmetric,  $H^+$ , and antisymmetric,  $H^-$ , contributions to the GPD  $H^q$  at  $\zeta = 0.18$  and  $t = t_{\min}$ . In this example,  $H^q$  was taken equal to zero in the DGLAP region.

$$H_{X < \zeta}^-(X, \zeta) = a^-(\zeta)X^2 - a^-(\zeta)\zeta X + H(\zeta, \zeta), \quad (45)$$

$$H_{X < \zeta}^+(X, \zeta) = a^+X^3 - a^+\zeta X^2 + cX + d, \quad (46)$$

where  $a^-(\zeta) = 6(\zeta H(\zeta, \zeta) - 2S_{\text{ERBL}})/\zeta^3$ ,  $S_{\text{ERBL}}$  being the area subtended by  $H_q^-$  in the ERBL region,

$$\begin{aligned} S_{\text{ERBL}} &= \int_0^\zeta dX H_q^-(X, \zeta, t) \\ &= \left(1 - \frac{\zeta}{2}\right) \left(F_1^q - \int_\zeta^1 \frac{H^q(X, \zeta, t)}{1 - \zeta/2} dX\right). \end{aligned} \quad (47)$$

$S_{\text{ERBL}}$  appears in the definition of  $a^-$  multiplied by a factor of 2 because of the crossing symmetry property for the areas subtended by  $H_q^-$  and  $H_q$ . In Eq. (46),  $a^+$  is a free parameter. This choice of parameters gives  $H_q = H^- = H^+$  at  $X = \zeta$ , the antiquark component in the DGLAP region being taken to be equal to zero in this phase of our analysis. Notice that  $H_q$  and  $H_{\bar{q}}$  are not required to obey crossing symmetries. They are obtained by construction from Eqs. (45) and (46). An example describing the symmetric and antisymmetric components of  $H^q$  is given in Fig. 4.

### III. RECURSIVE FIT: NUMERICAL EVALUATION OF GPD PARAMETERS FROM INCLUSIVE MEASUREMENT CONSTRAINTS

Here, we describe a recursive fitting procedure to extract the chiral-even GPDs from available DVCS data. Our fit uses the parametric forms (we omit the quark labels for simplicity)

$$F(X, \zeta, t) = \mathcal{N} G_{M_{x,m}}^{M_\Lambda}(X, \zeta, t) R_p^{\alpha, \alpha'}(X, \zeta, t), \quad (48)$$

TABLE I. Parameters obtained from our recursive fitting procedure applied to  $H_q$ ,  $E_q$ ,  $\tilde{H}_q$ , and  $\tilde{E}_q$ ;  $q = u, d$ . In a first phase, we fitted PDF global parametrizations in the valence quark sector and obtained  $m_q$ ,  $M_X^q$ ,  $M_\Lambda^q$ , and  $\alpha_q$ , as well as the normalization factor for  $H_q$ . Because we did not use the actual data at this stage, these parameters assume the fixed values in the table, with no error bar. We subsequently obtained  $\alpha'_q$ ,  $p_q$ , and the normalizations for  $E_q$ ,  $\tilde{H}_q$ , and  $\tilde{E}_q$  by fitting the proton and neutron electromagnetic form factors and the axial and pseudoscalar form factors, respectively [Eqs. (50)]. The value of the parameter in Eq. (34) is fixed at  $\beta = 10$ . Also shown are the  $\chi^2$  values for the separate contributions to the fit.

Parameters	$H$	$E$	$\tilde{H}$	$\tilde{E}$
$m_u$ (GeV)	0.420	0.420	2.624	2.624
$M_X^u$ (GeV)	0.604	0.604	0.474	0.474
$M_\Lambda^u$ (GeV)	1.018	1.018	0.971	0.971
$\alpha_u$	0.210	0.210	0.219	0.219
$\alpha'_u$	$2.448 \pm 0.0885$	$2.811 \pm 0.765$	$1.543 \pm 0.296$	$5.130 \pm 0.101$
$p_u$	$0.620 \pm 0.0725$	$0.863 \pm 0.482$	$0.346 \pm 0.248$	$3.507 \pm 0.054$
$\mathcal{N}_u$	2.043	1.803	0.0504	1.074
$\chi^2$	0.773	0.664	0.116	1.98
$m_d$ (GeV)	0.275	0.275	2.603	2.603
$M_X^d$ (GeV)	0.913	0.913	0.704	0.704
$M_\Lambda^d$ (GeV)	0.860	0.860	0.878	0.878
$\alpha_d$	0.0317	0.0317	0.0348	0.0348
$\alpha'_d$	$2.209 \pm 0.156$	$1.362 \pm 0.585$	$1.298 \pm 0.245$	$3.385 \pm 0.145$
$p_d$	$0.658 \pm 0.257$	$1.115 \pm 1.150$	$0.974 \pm 0.358$	$2.326 \pm 0.137$
$\mathcal{N}_d$	1.570	-2.800	-0.0262	-0.966
$\chi^2$	0.822	0.688	0.110	1.00

where  $F \equiv H, E, \tilde{H}, \tilde{E}$ ; the functions  $G_{M_X, m}^{M_\Lambda}$  are the covariant diquark contributions from Eqs. (27)–(30), and  $R_p^{\alpha, \alpha'}$  was given in Sec. II C.<sup>3</sup>

It should be remarked that our new parametric form follows from the one used in Refs. [24,25], while presenting several important differences. We have, first of all, completed a thorough analysis of the spin components of the various GPDs, both in the unpolarized and polarized sectors, thus releasing the assumption of a simplified quark-proton vertex structure made in [24,25] and extending our analysis to the much-needed  $\tilde{H}$  and  $\tilde{E}$  functions. The more careful spin treatment also results in a different shape for  $E$ , which, in [24,25], closely followed  $H$  by construction.

The most important features of our new parametrization are summarized below:

- (i) We consider only configurations for a spin-1/2 quark and a spin-0 diquark. The flexibility in shape contributed by considering a spin-1 diquark was, in fact, not sufficient to allow us to model, e.g., the rise at low  $X$ . We, therefore, opted for keeping the Regge term, as in [24,25]. This can, in fact, be derived from a ‘‘Reggeized’’ version of the model, as explained in Sec. II.
- (ii) We model *all* chiral-even GPDs and we present for the first time parametric forms for  $\tilde{H}$  and  $\tilde{E}$ , besides new evaluations for  $H$  and  $E$ . Our analysis applies to

the intermediate  $x_{Bj}$ , multi-GeV  $Q^2$  regime which is dominated by valence quarks in the DGLAP region. Only  $u$  and  $d$  quark flavors are considered.

- (iii) We perform a recursive fit in which parameters are evaluated orderly, from imposing constraints from DIS experimental results first, then from the elastic form factors, and eventually including DVCS data directly. This procedure affords us a better control on i) the number of parameters that are necessary to constrain the GPD multivariable problem and ii) the fit’s variants as new data are inserted.

All parameters obtained from the DIS and elastic constraints are given in Table I. They correspond to the first two steps of our fitting procedure. While we address in detail the impact of the GPDs  $H$ ,  $E$ , and  $\tilde{H}$  on the description of available DVCS data, we postpone the discussion of  $\tilde{E}$  to a dedicated analysis in [32]. As we explain, in what follows,  $\tilde{E}$  contributes to DVCS observables multiplied by a factor  $x_{Bj}$ , or  $\xi \approx x_{Bj}/(2 - x_{Bj})$ . As experimental data on DVCS target asymmetries accumulate, it is important to clarify that the pion pole contribution to  $\tilde{E}$  scales as  $1/x_{Bj}$  only in specific models like the chiral soliton-based factorized form described in Ref. [33]. While this factorized form is a convenient model, the  $\xi$  singularity is not required by the general analytic structure of the GPD. In fact, in our evaluation,  $\tilde{E}$  is estimated to be suppressed by a factor  $\lesssim 0.1$  at Hermes kinematics.

The first set of experimental constraints is given by the valence contribution to the inclusive DIS structure functions,

<sup>3</sup>In Appendix B, we present additional parametric forms that are more practical for applications and numerical calculations.

$$H^q(X, 0, 0, Q^2) = f_1^q(X, Q^2) \equiv q_v(X), \quad (49a)$$

$$\tilde{H}^q(X, 0, 0, Q^2) = g_1^q(X, Q^2) \equiv \Delta q_v(X), \quad (49b)$$

representing the forward limit of Eq. (48) (we have restored both the quark labels  $q = u, d$ , and for the  $Q^2$  dependence).  $f_1^q$  and  $g_1^q$  are obtained from DIS data. We do not use directly experimental data in this phase of the analysis, but we perform a fit of the valence components of existing parametrizations. The fit was performed similarly to Refs. [24,25]. By inspecting Eqs. (27), (29), and (48), one can see that, for  $t = 0$  and  $\zeta = 0$ , the only parameters that enter are  $M_X$ ,  $M_\lambda$ ,  $m$  in  $G_{M_X, m}^{M_\lambda}$ , and  $\alpha$  in  $R^{\alpha, \alpha'}$ .

We fit separately the unpolarized,  $H$ , and polarized,  $\tilde{H}$ , GPDs. For  $H$ , an additional parameter,  $\mathcal{N}$ , is fixed by the baryon number sum rules constraints,  $\int_0^1 dX u_v(X) = 2$  and  $\int_0^1 dX d_v(X) = 1$ . Therefore, in our first step, we have four parameters per distribution per quark flavor, giving a total number of parameters consistent with what was obtained in recent PDF parametrizations, e.g., [34–36]. As already noticed in [24–26], the diquark model-based parametrization corresponds to a low initial scale,  $Q_o^2$ . Parametric forms are then evolved to the  $Q^2$  of the data using LO perturbative QCD evolution equations [37]. Additional parameters not shown in the table are the initial value of the perturbative evolution scale,  $Q_o^2 = 0.0936 \text{ GeV}^2$ , and the parameters  $\beta$  appearing in Eq. (35),  $\beta = 10$ , and Eq. (36),  $\beta = 1.5$ . These were fixed by implementing directly DVCS data in our fit, as we will show in Sec. IV.

In the fit for  $\tilde{H}$ , we use a similar scheme as in current fits [38,39], where

$$X\Delta q_v(X, Q^2) = \mathcal{N}_q X^{-a_q} X q_v(X, Q^2).$$

We left the mass parameters  $M_X$  and  $M_\lambda$  fixed, as for the unpolarized case, while we varied  $\alpha$  and  $m$ . By letting the latter vary, we obtain the effect of the extra term  $\propto (1 + \gamma X)$  introduced in [39] for the LO fit. Figure 5 shows our curves for  $H_{u,d}(X, 0, 0)$  at the rather high value of  $Q^2 = 25 \text{ GeV}^2$ , in order to test the stability of our fit with perturbative QCD evolution. Other available PDF parametrizations from quantitative fits are also shown in the figure.

In the second phase of our fit, we impose an additional set of independent experimental constraints from the normalizations of the chiral-even GPDs to the nucleon form factors,

$$\int_0^1 H^q(X, \zeta, t) = F_1^q(t), \quad (50a)$$

$$\int_0^1 E^q(X, \zeta, t) = F_2^q(t), \quad (50b)$$

$$\int_0^1 \tilde{H}^q(X, \zeta, t) = G_A^q(t), \quad (50c)$$

$$\int_0^1 \tilde{E}^q(X, \zeta, t) = G_P^q(t), \quad (50d)$$

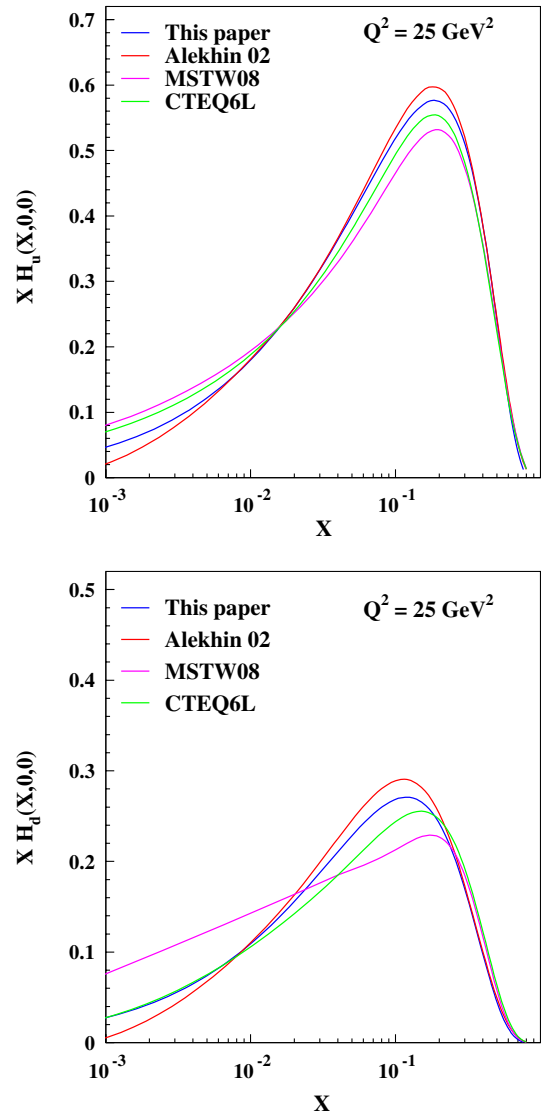


FIG. 5 (color online). GPDs  $H_u(X, 0, 0)$  (top) and  $H_d(X, 0, 0)$  (bottom), evaluated at  $Q^2 = 25 \text{ GeV}^2$ , compared with current LO parametrizations [34–36].

where  $F_1^q(t)$  and  $F_2^q(t)$  are the Dirac and Pauli form factors for the quark  $q$  components in the nucleon.  $G_A^q(t)$  and  $G_P^q(t)$  are the axial and pseudoscalar form factors.

Notice that the GPD  $\tilde{E}$  is constrained by the pseudoscalar form factor of the nucleon through Eq. (50). When the covariant or light front diquark spectator model is applied to calculating  $\tilde{E}(X, \zeta, t)$ , there is no kinematical singularity. The combination  $A_{+,+,-} + A_{-+,+}$  vanishes as  $\zeta \rightarrow 0$  for any  $X$  and  $t$ . This appears as a restriction on the GPD in the DGLAP region,  $X \geq \zeta$ . Requiring polynomiality leads to the sum rule in the ERBL region,

$$\int_0^\zeta \frac{dX}{1 - \zeta/2} \tilde{E}(X, \zeta, t) = G_P(t) - \int_\zeta^{+1} \frac{dX}{1 - \zeta/2} \tilde{E}(X, \zeta, t). \quad (51)$$

Since the integral in the DGLAP region is finite for any  $\zeta$  and does not have a pole at  $\zeta = 0$ , the ERBL region integral will not either. This will be true of any spectator model wherein there are no kinematic singularities introduced. In the diquark spectator approach that we use, the  $t$  dependence of the pion pole in the form factor can be reproduced while satisfying the sum rule in Eq. (51) (for small  $|t|$ ) by a suitable choice of mass and ‘‘Regge’’ parameters. This corresponds to a dual picture—a  $t$ -channel pion pole emerging from an integral over an  $s$ -channel diquark pole. In summary, we reiterate that the GPD  $\tilde{E}$  enters the target asymmetry always multiplied by  $\zeta(x_{Bj})$ , so that it contributes only weakly in the Hermes kinematical region.

Isospin decompositions allow one to relate the quark form factors to experimental measurements of  $F_{1(2)}^{p(n)}$ , the Dirac (Pauli) form factors for the proton (neutron), respectively.  $G_A$  and  $G_A^o$  are the isovector and isoscalar components of the axial nucleon form factor and  $G_P$ . We used the same selection of data as in Ref. [24] for the nucleon electromagnetic form factors (see references in [40]). The resulting parameters are given in Table I. More recent data [41] are now available that show a milder slope of the electric to magnetic proton form factor ratio at large  $|t|$ . However, these do not largely affect our fits that are limited to the  $-t \ll Q^2 \approx 2\text{--}3 \text{ GeV}^2$  region.  $G_A$  is obtained from the global average of neutron beta decay and neutrino scattering experiments (see Ref. [42] and references therein),

$$G_A(t) = \frac{g_A}{(1 - \frac{t}{M_A^2})^2}, \quad (52)$$

with  $g_A = 1.2695 \pm 0.0029$  and  $M_A = 1.026 \pm 0.021 \text{ GeV}$ .  $G_P$  is notoriously dominated by a pion pole contribution, a small nonpion pole component being also present. We used the experimental values displayed, e.g., in Ref. [43]. A more thorough discussion of this form factor will be given in [32].

As a result, for each quark flavor and GPD type, using the constraints above, we can determine the additional parameters,  $\alpha'$  and  $p$  in Eq. (48), and the normalizations  $\mathcal{N}$  [Eq. (48) and Table I]. The number of parameters used is consistent with the one used in fits of the nucleon form factor data. These require four parameters for  $G_E^p$ ,  $G_M^p$ , and  $G_M^n$ , respectively, and two for  $G_E^n$  [40,44].

The GPDs  $H_{u,d}(X, 0, 0)$ ,  $E_{u,d}(X, 0, 0)$ , and  $\tilde{H}_{u,d}(X, 0, 0)$  are shown in Fig. 6 both at the initial scale,  $Q_o^2$ , and evolved to  $Q^2 = 2 \text{ GeV}^2$ . A comparison with results on  $H^q$  and  $E^q$  from [24,25] at the scale  $Q_o^2$  is also shown. In Fig. 7, we show  $H_{u,d}(X, \zeta, t; Q^2)$  evaluated at  $Q^2 = 2 \text{ GeV}^2$  and for a variety of ranges in  $\zeta \equiv x_{Bj}$  and  $Q^2$ . In Fig. 8, we show the working of the property of polynomiality. This is, in a nutshell, a direct consequence of extending the operator product expansion to the off-forward case [5,45], according to which the Mellin moments of GPDs read (see also [46])

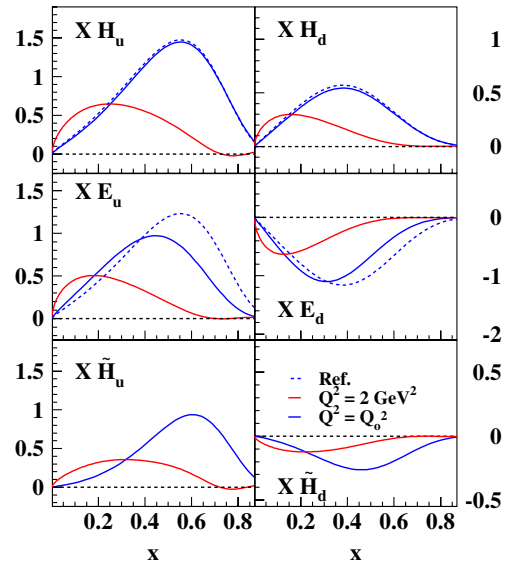


FIG. 6 (color online). GPDs  $F_q(X, 0, 0) \equiv \{H_q, E_q, \tilde{H}_q\}$ , for  $q = u$  (left) and  $q = d$  (right), evaluated at the initial scale,  $Q_o^2 = 0.0936 \text{ GeV}^2$ , and at  $Q^2 = 2 \text{ GeV}^2$ , respectively. The dashed lines were calculated using the model in Refs. [24,25] at the initial scale.

$$\begin{aligned} H_n^q(\xi, t) &= \int_{-1}^1 H_q(x, \xi, t) x^{n-1} dx \\ &= A_{n0}(t) + A_{n,2}(t)(2\xi)^2 + \dots + A_{n,n-1}(t)(2\xi)^{n-1}, \end{aligned} \quad (53)$$

where  $n \geq 1$ , and only even powers of  $\xi$  are included. Similar results hold for  $E_q$ ,  $\tilde{H}_q$ , and  $\tilde{E}_q$  [46]; for  $n > 1$ , the equation is also  $Q^2$ -dependent. To illustrate polynomiality, the moments of  $H_u$  were plotted vs  $\xi$  at the initial scale,  $Q_o^2$ , for different values of  $t$ , and for  $n \leq 5$  (the trend shown in Fig. 8 holds for even larger values of  $n$ ). The two sets of curves represent the calculation using the parametrization from this paper and the results of a polynomial fit in  $\xi^2$ . Clearly, our parametrization satisfies the property of polynomiality, although this cannot be inferred directly from the functional form in Eq. (48).

To summarize, we proceeded through two steps of our recursive fit. We used the flexible model described in Sec. II to first fit the nucleon unpolarized and polarized PDFs, respectively, by using all parameters that enter the expressions at  $t = 0$  and  $\zeta = 0$ . We subsequently fitted the nucleon electromagnetic and electroweak form factors using the additional parameters that enter at  $t \neq 0$  and  $\zeta = 0$ . At this stage of the analysis, we established that, in order to obtain GPDs that are constrained by a set of parameters which is consistent with the ones used for independent fits of the DIS structure functions and of the nucleon form factors, a total number of 4 (DIS) plus 3 (Elastic) parameters per quark flavor per GPD is needed. The number of parameters is, in practice, reduced because of the physically motivated ansatz introduced in our approach, as one

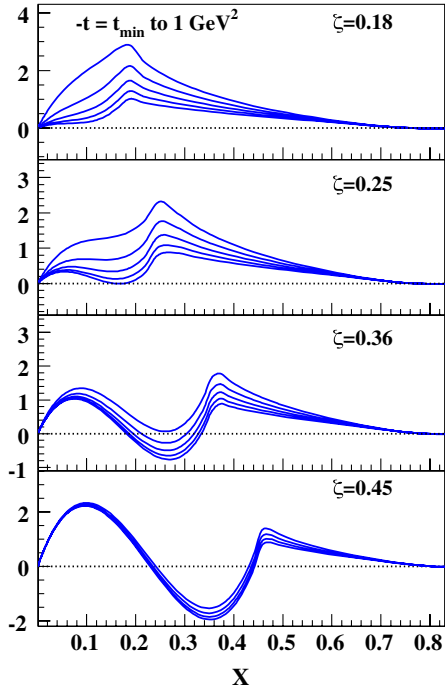


FIG. 7 (color online).  $H_u(X, \zeta, t; Q^2)$  evaluated at  $Q^2 = 2 \text{ GeV}^2$ . Each panel shows  $H_u$  plotted vs  $X$  at different values of  $\zeta = 0.18, 0.25, 0.36, 0.45$ . For each value of  $\zeta$ , several curves are shown that correspond to a range of values in  $-t$  from  $t_{\min} = -M^2 \zeta^2 / (1 - \zeta)$  to  $1 \text{ GeV}^2$ .

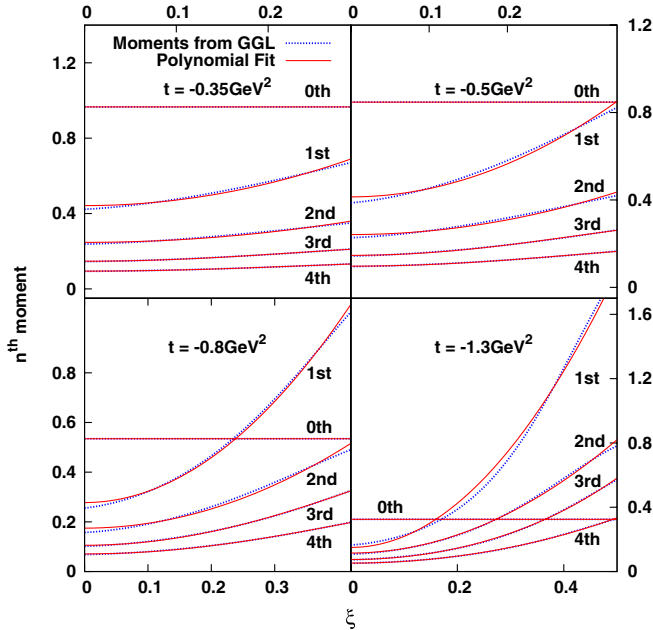


FIG. 8 (color online). The polynomiality property in our parametrization. The dashed lines are the theoretical results using the parametrization from this paper; the solid lines correspond to a polynomial fit in  $\xi^2$  to the theoretical curves. The two sets of curves display an excellent agreement with each other, thus demonstrating that polynomiality is satisfied in our model.

can see by inspecting the values in Table I. Physical assumptions are both useful to understand the trend of data and, at the same time, they are known to introduce a bias. This aspect is well-known to affect all hard process multivariable analyses and it can be perhaps overcome in suitable neural network-based approaches [47,48].

The third set of experimental constraints is given by DVCS-type data. In our analysis, we use strictly DVCS data that are cleaner from the theoretical point of view, as compared to deeply virtual meson production. By fitting the CFFs that are functions of  $\zeta$ ,  $t$ , and  $Q^2$ , we will be able to provide a constraint on the otherwise elusive  $\zeta$  dependence of the GPDs. To understand how many extra parameters are needed in extending the fit to its third phase, we devised a procedure explained in the following section.

#### IV. IMPLEMENTATION OF DVCS DATA

We now discuss our procedure to extract GPDs from available DVCS data. Fully quantitative studies were performed in [16,17], where a number of observables were fitted that were obtained from experimental data for the process  $ep \rightarrow ep\gamma$  from both Hermes and Jefferson Lab. In order to have a consistent comparison, we included in our analysis a similar set of observables. Below, we list their expressions in terms of the CFFs displayed in Secs. II and III. In order to proceed, we first introduce the helicity formalism. This method allows us to obtain a physical interpretation of the various structures and azimuthal angular dependences involved, in terms of the photon helicity states.

##### A. Observables

The observables included in our fit are from all the DVCS measurements that were available to us, to date. These are the cross section for unpolarized electron scattering,  $d\sigma/d\Phi$  [49,50], the beam spin asymmetry,  $A_{LU}$  [49,51], the beam charge asymmetry,  $A_C$  [52], and the transverse spin asymmetries,  $A_{UT}^{\text{DVCS}}$  and  $A_{UT}^I$  [52,53]. The cross section for scattering of an electron/positron beam with polarization  $h$  off a proton target is evaluated considering the sum of the DVCS and Bethe-Heitler (BH) amplitudes,

$$\frac{d^5\sigma^h}{dQ^2 dx_{Bj} dt d\phi d\phi_N} = \Gamma |T_{\text{BH}} + T_{\text{DVCS}}|^2, \quad (54)$$

where the factor  $\Gamma$  is given by

$$\Gamma = \frac{\alpha^3}{16\pi^2} \frac{x_{Bj} y}{Q^2 (2Mx_{Bj}\epsilon_1)} \frac{1}{\sqrt{1 + \epsilon^2}}$$

with  $y = \nu/\epsilon_1$ ,  $\epsilon_1$  being the initial electron energy and  $\nu = \epsilon_1 - \epsilon_2$  the momentum transfer;  $\epsilon = 4M^2 x_{Bj}^2 / Q^2$ ; and  $\phi$  is the (azimuthal) angle between the hadronic and leptonic planes in the frame where the virtual photon's momentum is along the  $z$  axis [10]. The unobserved

helicities have been summed over implicitly.<sup>4</sup> The various observables that we consider are written as

$$\frac{d\sigma}{d\Phi} = \frac{1}{2} \left[ \frac{d^4\sigma^\uparrow}{d\Phi} + \frac{d^4\sigma^\downarrow}{d\Phi} \right] = \Gamma(|T_{\text{BH}}|^2 + |T_{\text{DVCS}}|^2 + I), \quad (55)$$

$$A_{LU} = \frac{\frac{d^4\sigma^\uparrow}{d\Phi} - \frac{d^4\sigma^\downarrow}{d\Phi}}{\frac{d^4\sigma^\uparrow}{d\Phi} + \frac{d^4\sigma^\downarrow}{d\Phi}} = \frac{I^\uparrow - I^\downarrow}{|T_{\text{BH}}|^2 + |T_{\text{DVCS}}|^2 + I}, \quad (56)$$

$$A_C = \frac{\frac{d^4\sigma^+}{d\Phi} - \frac{d^4\sigma^-}{d\Phi}}{\frac{d^4\sigma^+}{d\Phi} + \frac{d^4\sigma^-}{d\Phi}} = \frac{I}{|T_{\text{BH}}|^2 + |T_{\text{DVCS}}|^2}, \quad (57)$$

$$A_{UT}^{\text{DVCS}} = \frac{1}{S_\perp} \frac{(\frac{d^4\sigma_{\perp}^+}{d\Phi} - \frac{d^4\sigma_{\perp}^-}{d\Phi}) + (\frac{d^4\sigma_{\parallel}^-}{d\Phi} - \frac{d^4\sigma_{\parallel}^+}{d\Phi})}{\frac{d^4\sigma^+}{d\Phi} + \frac{d^4\sigma^-}{d\Phi}} = \frac{|T_{TP}^{\text{DVCS}}|^2}{|T_{\text{BH}}|^2 + |T_{\text{DVCS}}|^2}, \quad (58)$$

$$A_{UT}^I = \frac{1}{S_\perp} \frac{(\frac{d^4\sigma_{\perp}^+}{d\Phi} - \frac{d^4\sigma_{\perp}^-}{d\Phi}) - (\frac{d^4\sigma_{\parallel}^-}{d\Phi} - \frac{d^4\sigma_{\parallel}^+}{d\Phi})}{\frac{d^4\sigma^+}{d\Phi} + \frac{d^4\sigma^-}{d\Phi}} = \frac{I_{TP}}{|T_{\text{BH}}|^2 + |T_{\text{DVCS}}|^2}, \quad (59)$$

where  $d\Phi \equiv d\phi dx_{Bj} dt dQ^2$ ; the superscripts  $(-)$  refer to the beams' charge;  $\uparrow$  ( $\downarrow$ ) are for oppositely polarized electron beams; and the subscripts  $\Leftarrow$  ( $\Rightarrow$ ) represent the transverse target polarizations, corresponding to the angles  $\phi_S$  and  $\phi_S + \pi$ , respectively. The subscript  $TP$  follows the notation of [10] for a transverse polarized target; the subscript  $LU$  is for a longitudinally polarized beam,  $L$ , and an unpolarized target,  $U$ , while  $UT$  is for an unpolarized beam and a transversely polarized target.

An expression for  $T_{\text{BH}}$ , the amplitude for the BH process, is given in Ref. [10]. Here, we write the amplitude in helicity basis in order to facilitate the expansion of the observables in bilinear products of amplitudes and GPDs. The basic form of the BH amplitude is

$$T_{\text{BH}}^{h,\Lambda,\Lambda',\Lambda'_\gamma} = L_{\mu\kappa}^h \epsilon^{*\kappa\Lambda'_\gamma} \frac{1}{Q^2} J_{\Lambda,\Lambda'}^\mu, \quad (60)$$

where

$$L_{\mu\kappa}^h = \bar{u}(k_2, h) [\gamma_\mu (\gamma_\rho [k_1^\rho - q^\rho])^{-1} \gamma_\kappa + \gamma_\kappa (\gamma_\rho [k_2^\rho + q^\rho])^{-1} \gamma_\mu] u(k_1, h) \quad (61)$$

and

<sup>4</sup>Comparisons with experiments require a rotation of the angles given above from the Belitsky-Kirchner-Mueller [10] frame to either the Lab frame or the  $ep$  center-of-mass frame corresponding, respectively, to Jefferson Lab and Hermes experiments.

$$J_{\Lambda,\Lambda'}^\mu = \bar{U}(p', \Lambda') \left[ F_1(\Delta^2) \gamma^\mu + i \frac{\sigma^{\mu,\tau} \Delta_\tau}{2M} F_2(\Delta^2) \right] U(p, \Lambda). \quad (62)$$

The DVCS amplitude for scattering of a lepton with helicity  $h$  is given by

$$T_{\text{DVCS}}^{h,\Lambda,\Lambda',\Lambda'_\gamma} = \bar{u}(k_2, h) \gamma_\mu u(k_1, h) \frac{1}{Q^2} T_{\Lambda,\Lambda'}^{\mu\nu} \epsilon_\nu^{*\Lambda'_\gamma}, \quad (63)$$

where  $u(k_{1(2)}, h)$  are the initial and final lepton spinors; the hadronic tensor,  $T_{\Lambda,\Lambda'}^{\mu\nu}$ , was defined in Sec. II, and  $\epsilon_\nu^{*\Lambda'_\gamma}$  is the outgoing photon polarization vector.  $T_{\text{DVCS}}$  can be expressed in terms of helicity amplitudes by considering the following expansion on the polarization vector basis [54,55],

$$T_{\text{DVCS}}^{h,\Lambda,\Lambda',\Lambda'_\gamma} = A_h^+ f_{+, \Lambda; \Lambda', \Lambda'} + A_h^- f_{-, \Lambda; \Lambda', \Lambda'} + \frac{\sqrt{Q^2}}{\nu} A_h^3 f_{0, \Lambda; \Lambda', \Lambda'}, \quad (64)$$

with

$$A_h^\pm = \frac{\pm 1}{\sqrt{Q^2}} \left( \sqrt{\frac{1+\epsilon}{2(1-\epsilon)}} \mp h\sqrt{2} \right) e^{\pm i\phi} = \mp \frac{1}{\sqrt{2}} \bar{u}(k_2, h) [\gamma_1 \pm i\gamma_2] u(k_1, h), \quad (65a)$$

$$\frac{\sqrt{Q^2}}{\nu} A_h^3 = \frac{\nu}{Q^2} \sqrt{\frac{2\epsilon}{1-\epsilon}} = \bar{u}(k_2, h) \gamma_3 u(k_1, h). \quad (65b)$$

The  $f$  amplitudes were given in terms of CFFs in Sec. II. At LO, by disregarding the longitudinal photon polarization, the only amplitudes that were found to contribute are  $f_{+,+,+,+}$ ,  $f_{-+,-,+}$ ,  $f_{+,+,-}$ , and  $f_{-+,-,-}$  [see Eqs. (15)]. As a consequence, the only term contributing to the unpolarized term,  $|T_{\text{DVCS}}|^2$ , and corresponding to the transverse cross section,  $d\sigma_T/dt$ , is given by

$$|T_{\text{DVCS}}|^2 = \frac{1}{Q^2} \frac{1}{2(1-\epsilon)} (|f_{+,+,+,+}|^2 + |f_{-+,-,+}|^2 + |f_{+,+,-}|^2 + |f_{-+,-,-}|^2). \quad (66)$$

In terms of CFFs,

$$|T_{\text{DVCS}}|^2 = \frac{1}{Q^2} \frac{1}{2(1-\epsilon)} \frac{1}{(2-x_{Bj})^2} \times \left[ 4(1-x_{Bj})(\mathcal{H}^* \mathcal{H} + \tilde{\mathcal{H}}^* \tilde{\mathcal{H}}) - x_{Bj}^2 (\mathcal{E}^* \mathcal{H} + \mathcal{H}^* \mathcal{E} + \tilde{\mathcal{E}}^* \tilde{\mathcal{H}} + \tilde{\mathcal{H}}^* \tilde{\mathcal{E}}) - 4 \left( \frac{x_{Bj}^2}{1-x_{Bj}} + \frac{t}{4M^2} \right) \mathcal{E}^* \mathcal{E} - 4x_{Bj}^2 \frac{t}{4M^2} \tilde{\mathcal{E}}^* \tilde{\mathcal{E}} \right]. \quad (67)$$

Equation (67) is analogous to the term  $c_0^{\text{DVCS}}$  in the expansion given in [10]. Note that the sum over all the unobserved helicities is implicit.

An analogous decomposition into the virtual photon polarization basis for the Bethe-Heitler amplitude of Eq. (60) has the form

$$T_{\text{BH}}^{h,\Lambda,\Lambda',\Lambda'_\gamma} = B_{h,\Lambda'_\gamma}^+ J_{+,\Lambda;\Lambda'} + B_{h,\Lambda'_\gamma}^- J_{-,\Lambda;\Lambda'} + \frac{\sqrt{Q^2}}{\nu} B_{h,\Lambda'_\gamma}^0 J_{0,\Lambda;\Lambda'}. \quad (68)$$

The hadronic amplitudes are

$$J_{\pm 1,\Lambda;\Lambda'=\Lambda} = -\frac{p'_\perp}{\sqrt{1-\xi^2}} F_2(t),$$

$$J_{\pm 1,\Lambda;\Lambda'=-\Lambda} = \Lambda \frac{(p'_\perp)^2}{2M\sqrt{1-\xi^2}} F_2(t) + \delta_{\Lambda,\pm} \frac{\sqrt{2}M\xi}{\sqrt{1-\xi^2}} (F_1(t) + F_2(t)), \quad (69)$$

where terms of order  $(\Delta_\perp/p^+)^2$  and  $(M/p^+)^2$  were dropped.

The lepton tensor for the Bethe-Heitler amplitude can be calculated from Eq. (61) using the relation

$$\gamma^\mu \gamma^\nu \gamma^\rho = g^{\mu\nu} \gamma^\rho + g^{\nu\rho} \gamma^\mu - g^{\rho\mu} \gamma^\nu - i\epsilon^{\mu\nu\rho\sigma} \gamma_\sigma \gamma_5. \quad (70)$$

Momentum conservation gives the exchanged virtual photon momentum as  $q_X = k_2 + q' - k_1 = q' - q = q' - (p - p') = q' - \Delta$ . It can be seen that the Dirac algebra is reduced to evaluating a single  $\gamma^\sigma$  or  $\gamma^\sigma \gamma^5$ .

The interference term is given by

$$I = \sum_{h,\Lambda,\Lambda',\Lambda'_\gamma} (T_{\text{BH}}^{*h,\Lambda,\Lambda',\Lambda'_\gamma} T_{\text{DVCS}}^{h,\Lambda,\Lambda',\Lambda'_\gamma} + T_{\text{DVCS}}^{*h,\Lambda,\Lambda',\Lambda'_\gamma} T_{\text{BH}}^{h,\Lambda,\Lambda',\Lambda'_\gamma}). \quad (71)$$

We consider the following expansion over helicity states of  $T_{\text{BH}}^{h,\Lambda,\Lambda',\Lambda'_\gamma}$  and  $T_{\text{DVCS}}^{h,\Lambda,\Lambda',\Lambda'_\gamma}$  in terms of  $f_{\Lambda,\Lambda;\Lambda',\Lambda'}$  for fixed lepton helicity  $h$ ,

$$I^h = [([B_{h,+1}^{+1*} J_{+1;+,+} + B_{h,+1}^{0*} J_{0;+,+} + B_{h,+1}^{-1*} J_{-1;+,+}] A_h^{+1} + [B_{h,-1}^{+1*} J_{-1;+,+} + B_{h,-1}^{0*} J_{0;+,+} + B_{h,-1}^{-1*} J_{+1;+,+}] A_h^{-1}) f_{+,+,+} + ([B_{h,-1}^{+1*} J_{+1;+,+} + B_{h,-1}^{0*} J_{0;+,+} + B_{h,-1}^{-1*} J_{-1;+,+}] A_h^{-1} + [B_{h,+1}^{+1*} J_{+1;+,+} + B_{h,+1}^{0*} J_{0;+,+} + B_{h,+1}^{-1*} J_{-1;+,+}] A_h^{+1}) f_{-,+,-}], \quad (72)$$

$$+ [B_{h,+1}^{+1*} J_{-1;+,+} + B_{h,+1}^{0*} J_{0;+,+} + B_{h,+1}^{-1*} J_{+1;+,+}] A_h^{+1} f_{-,+,-} + [([B_{h,+1}^{+1*} J_{+1;+,-} + B_{h,+1}^{0*} J_{0;+,-} + B_{h,+1}^{-1*} J_{-1;+,-}] A_h^{+1} + [B_{h,-1}^{+1*} J_{+1;+,-} - B_{h,-1}^{0*} J_{0;+,-} - B_{h,-1}^{-1*} J_{+1;+,-}] A_h^{-1}) f_{+,+,-}, \quad (73)$$

$$+ ([B_{h,-1}^{+1*} J_{+1;+,-} + B_{h,-1}^{0*} J_{0;+,-} + B_{h,-1}^{-1*} J_{-1;+,-}] A_h^{-1}, \quad (74)$$

$$+ [B_{h,+1}^{+1*} J_{+1;-,+} - B_{h,+1}^{0*} J_{0;-,+} - B_{h,+1}^{-1*} J_{+1;-,+}] A_h^{+1} f_{-,+,-}], \quad (75)$$

where the various helicity-dependent terms are defined in Eqs. (61), (69), and (64).

We then cast Eq. (71) in a form analogous to the structure of the leading terms in the expansion of Ref. [10],<sup>5</sup>

$$I = \sum_h I^h = \sum_h (c_0^I + c_1^I \cos\phi + h s_1^I \sin\phi), \quad (76)$$

with coefficients given by

$$c_0^I = -8 \frac{(2-y)^3}{1-y} K^2 \left[ F_1 \Re e \mathcal{H} + \frac{x_{Bj}}{2-x_{Bj}} (F_1 + F_2) \Re e \tilde{\mathcal{H}} - \frac{t}{4M^2} F_2 \Re e \mathcal{E} \right], \quad (77)$$

$$c_1^I = -8(2-2y+y^2) K \left[ F_1 \Re e \mathcal{H} + \frac{x_{Bj}}{2-x_{Bj}} (F_1 + F_2) \Re e \tilde{\mathcal{H}} - \frac{t}{4M^2} F_2 \Re e \mathcal{E} \right], \quad (78)$$

$$s_1^I = 8y(2-y) K \left[ F_1 \Im m \mathcal{H} + \frac{x_{Bj}}{2-x_{Bj}} (F_1 + F_2) \Im m \tilde{\mathcal{H}} - \frac{t}{4M^2} F_2 \Im m \mathcal{E} \right]. \quad (79)$$

The kinematical factor  $K$  is, at leading order in  $-t/Q^2$ ,

$$K = \left[ \frac{-t}{Q^2} (1-x_{Bj}) \left( 1-y - \frac{y^2 \epsilon^2}{4} \right) \left( 1 - \frac{t_{\min}}{t} \right) (1+\epsilon)^{1/2} \right]^{1/2},$$

with  $t_{\min} = -x_{Bj}^2 / (1-x_{Bj}) M^2$ .

For a practical approach, we streamline both the kinematical dependence and the GPD content of the various

<sup>5</sup>Note that  $I$  has been written for electron scattering. For positron scattering as, e.g., in  $A_C$ ,  $I$  appears with a negative sign. This underlines the forms displayed in Eqs. (55)–(58) and (84).

observables. By keeping the leading terms in  $-t/Q^2$  and in  $x_{Bj}$ , we obtain

$$\frac{d\sigma}{d\Phi} = \Gamma(B(\phi) + C(\phi) \cos\phi), \quad (80)$$

$$A_{LU} = \frac{A(\phi) \sin\phi}{B(\phi) + C(\phi) \cos\phi}, \quad (81)$$

$$A_{UT}^I = \frac{(F(\phi) + G(\phi) \cos\phi) \sin(\phi - \phi_S) + H(\phi) \cos(\phi - \phi_S) \sin\phi}{B(\phi) - D(\phi)}, \quad (84)$$

where the coefficients  $A$  to  $H$  are presented in combinations of factorized forms isolating the kinematical factors  $K_{I,\text{DVCS}}^I$  from the dynamical parts,

$$A = K_I^1(\phi) \Im m C_I, \quad (85a)$$

$$B = C_{\text{BH}}^0(\phi) + K_{\text{DVCS}}^0 C_{\text{DVCS}} + K_I^0(\phi) \Re e C_I, \quad (85b)$$

$$C = K_I^2(\phi) \Re e C_I, \quad (85c)$$

$$D = K_I^0(\phi) \Re e C_I, \quad (85d)$$

$$E = K_{\text{DVCS}}^{UT} C_{\text{DVCS}}^{UT}, \quad (85e)$$

$$F = \frac{-t}{Q^2} K_I^{UT}(\phi) C_{I,0}^{UT}, \quad (85f)$$

$$G = K_I^{UT}(\phi) C_{I,0}^{UT}, \quad (85g)$$

$$H = K_I^{UT}(\phi) C_{I,1}^{UT}. \quad (85h)$$

$C_{\text{BH}}^0(\phi)$  defines the BH cross section and is given, e.g., in [10]. The kinematical factors depend on  $t$ ,  $x_{Bj}$ ,  $y$ ,  $Q^2$ , and  $\epsilon$  (we give their expressions in Appendix D); notice that, for the BH and interference terms, there is an extra dependence on  $\phi$  due to the presence of the BH propagators. At leading order, i.e., disregarding terms multiplied by  $x_{Bj}^2$ ,  $x_{Bj}t$ , one has

$$C_I = F_1 \mathcal{H} + \frac{x_{Bj}}{2 - x_{Bj}} (F_1 + F_2) \tilde{\mathcal{H}} - \frac{t}{4M^2} F_2 \mathcal{E}, \quad (86)$$

$$C_{\text{DVCS}} = \Re e^2 \mathcal{H} + \Im m^2 \mathcal{H} + \Re e^2 \tilde{\mathcal{H}} + \Im m^2 \tilde{\mathcal{H}}, \quad (87)$$

$$C_{\text{DVCS}}^{UT} = \Re e \mathcal{E} \Im m \mathcal{H} - \Re e \mathcal{H} \Im m \mathcal{E}, \quad (88)$$

$$C_{I,0}^{UT} = \frac{t}{4M^2} (2 - x_{Bj}) F_1 \Im m \mathcal{E} - \frac{t}{M^2} \frac{1 - x_{Bj}}{2 - x_{Bj}} F_2 \Im m \mathcal{H}, \quad (89)$$

$$C_{I,1}^{UT} = (1 - x_{Bj}) \frac{t}{M^2} F_2 \Im m \tilde{\mathcal{H}}. \quad (90)$$

## B. Fit results

We present results from our fit, including all parameters that were fixed using the Reggeized diquark parametrization described in Secs. II and III and displayed in Table I.

$$A_C = \frac{D(\phi) + C(\phi) \cos\phi}{B(\phi) - D(\phi)}, \quad (82)$$

$$A_{UT}^{\text{DVCS}} = \frac{E(\phi) \sin(\phi - \phi_S)}{B(\phi) - D(\phi)}, \quad (83)$$

We introduce additional flexibility through extra parameters entering Eq. (34) in order to constrain the  $\zeta$  dependence from all available DVCS data. Although, in principle, as many  $\beta$  parameters as the number of flavors and GPDs could be introduced, given the small data set presently available, we use one value of  $\beta$  for all GPDs. More accurate studies including flavor and GPD-dependent  $\beta$  parameters will be conducted as more data become available. In Fig. 9, we show the real and imaginary parts of the CFFs,  $\mathcal{H}(\zeta, t)$ , appearing in Eqs. (85). Similar results are obtained for  $E$ ,  $\tilde{H}$ , and  $\tilde{E}$ . One can see that the slope in  $\zeta$  flattens out as  $-t$  increases.

Our fit uses the two currently available sets of data, from both Hall A and Hall B collaborations at Jefferson Lab, and the Hermes Collaboration, respectively. Since the kinematical ranges covered by the two experiments only

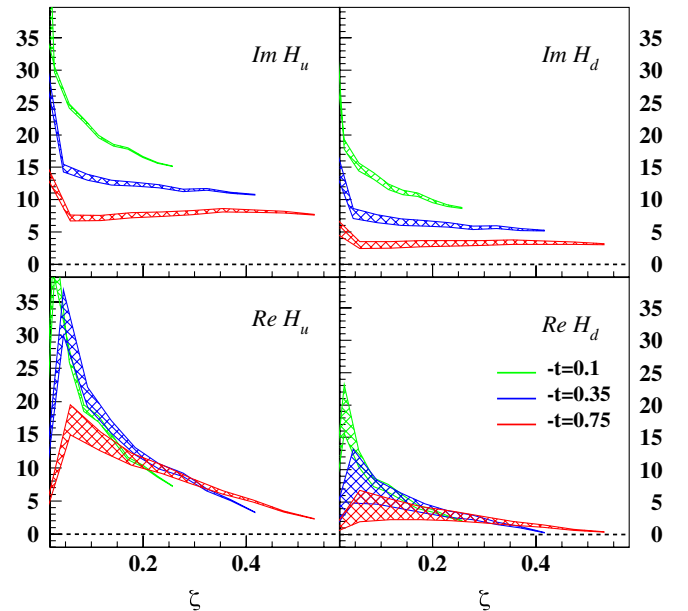


FIG. 9 (color online). Real and imaginary parts of the CFFs,  $\mathcal{H}_i(\zeta, t)$ , entering Eqs. (85). The CFFs are plotted vs  $x_{Bj} \equiv \zeta$ , for different values of  $t$ , at  $Q^2 = 2 \text{ GeV}^2$ . They are shown with the theoretical uncertainty from the parameters in Table I. Similar results are obtained for  $E$  and  $\tilde{H}$ .

partially overlap, in this first step, we start by fitting the Jefferson Lab set and subsequently extend the results of our fit to predict the behavior of the Hermes set.

### 1. Jefferson Lab data

The DVCS data on  $A_{LU}$  from Hall B [51] and on the sum and the difference of the beam polarization cross sections from Hall A [49] were implemented directly in our fit. This allows us to constrain the parameter  $\beta$ . In Figs. 10 and 11, we show the results of our fits using the quantity  $A_{LU}(90^\circ) = A/B$ , Eq. (81). The experimental points in the figure were obtained by fitting  $A_{LU}(\phi)$  in the 12 bins displayed in Ref. [51] (Fig. 4). The statistical and systematic errors were added in quadrature, and no error correlations were considered (this is giving rise in our case to larger error bands, although the central points coincide with the ones in Ref. [51]). A similar procedure

was used for the Hall A data that are also displayed in the figures. The dashed lines in both figures are a prediction of the fit using only the PDFs and form factor constraints. Clearly, by taking only these constraints, the  $\zeta$  slope of the CFFs is unconstrained and evidently off the data trend, as it can be seen in the larger  $\zeta \equiv x_{Bj}$  bins. The additional term in Eq. (34) can regulate this behavior. Two possible ways of implementing it are shown, respectively, by the full lines in the two figures. In Fig. 10, a multiplicative term was considered only in the numerator of the asymmetry, given by  $A$ . In Fig. 11, the zeta-dependent factor was introduced in the GPDs and used to calculate the CFFs in both the numerator and denominator of the asymmetry. The effect of introducing such terms in the GPDs gives a different dependence that can be ascribed to modifying both the real and imaginary parts of the CFFs. We show results using two different expressions for  $\beta$ , Eqs. (35) and (36), in order to illustrate some of the subtleties that are involved in the extraction of the CFFs and GPDs from the data. While the two expressions give almost identical results for the asymmetry, they impact the various terms— $A$ ,  $B$ , and  $C$  in Eqs. (85)—in different ways. With more data in hand, including a separation of the absolute cross sections, one will be able to perform precise fits of the behavior in  $\zeta$ .

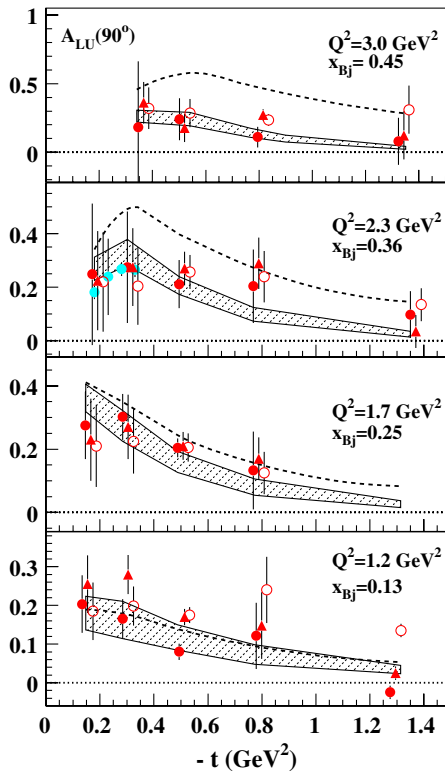


FIG. 10 (color online). Beam spin asymmetry,  $A_{LU}(\phi = 90^\circ)$ , in 12 of the  $x_{Bj}$  and  $Q^2$  bins measured in Hall B [51]. The data points were extracted by fitting  $A_{LU}(\phi)$ ; however, they do not represent the uncertainties reported in the experimental analysis. The second panel from the top includes also data from Hall A [49]. The full circles, open circles, and triangles represent data in similar  $x_{Bj}$  and  $t$  bins, but at  $Q^2$  values slightly displaced around the value reported in the legend. All curves were obtained at the kinematics displayed in the figure. Dashed lines: results from the fit using only the PDF and form factor constraints as from Table I. The solid lines represent the effect of introducing the  $\zeta$ -dependent term, Eq. (34), in the numerator of the asymmetry only.

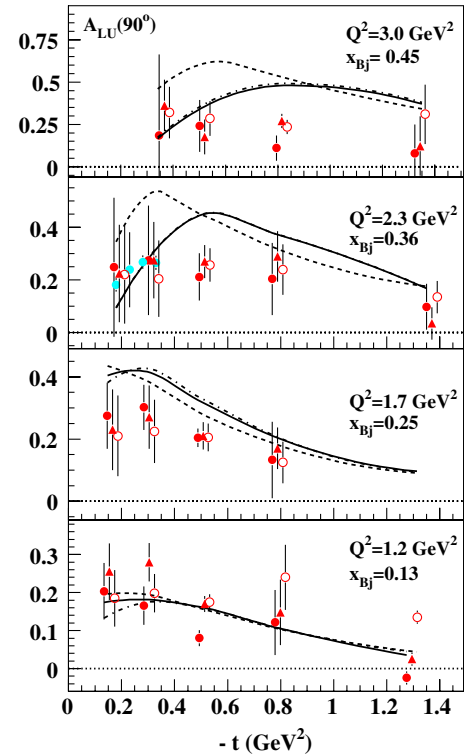


FIG. 11 (color online). Experimental data: same as Fig. 10. Dashed lines: results from the fit using only the PDF and form factor constraints as from Table I. The effect of the  $\zeta$ -dependent terms given in Eq. (35) and (36) is given by the solid lines and the dot-dashed lines, respectively.

In Figs. 12–15, we analyze the effect of the different GPD components on the fit to Hall B data. Figure 12 shows the contribution of the BH term and of the coefficients  $A$  and  $B$  from Eqs. (85), with the  $\zeta$ -dependent term from Eq. (35) (lines with bullets) and without it (lines with no bullets). Figure 13 shows the separate contributions of the numerator and denominator,  $A$ , and  $B$ , Eqs. (85), to the ratio defining the asymmetry  $A_{LU}(90^\circ)$ .  $B$  is given by the sum of the three terms displayed in the figure. Notice that the real part of the CFFs enters only  $T_{\text{DVCS}}^2$ , which is a

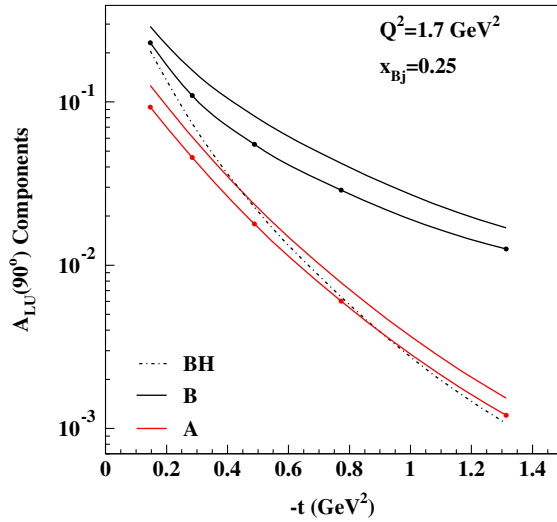


FIG. 12 (color online). Contribution of the BH term (dot-dashed line) and of the coefficients  $A$  and  $B$  from Eqs. (85) with the  $\zeta$ -dependent term from Eq. (35) (lines with bullets), and without it (lines with no bullets), at  $Q^2 = 1.7 \text{ GeV}^2$  and  $x_{Bj} = 0.25$ . Similar results are obtained in other kinematics.

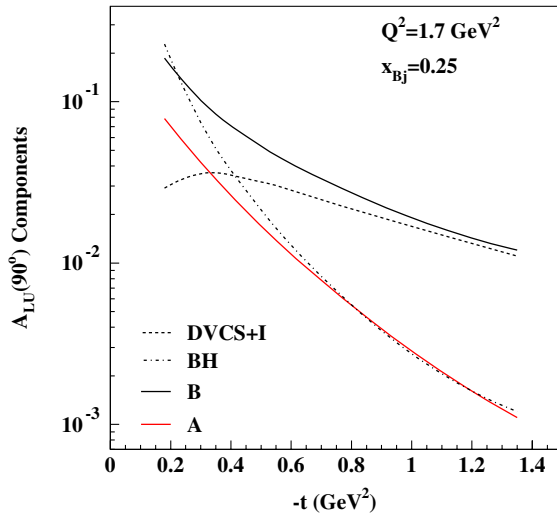


FIG. 13 (color online). Separate contributions of the numerator and denominator,  $A$  and  $B$ , Eqs. (85), to the  $A_{LU}(90^\circ)$ .  $B$  is given by the BH term (dot-dashed line) plus the sum of the  $|T_{\text{DVCS}}|^2$  and interference terms (dashed line).  $Q^2 = 1.7 \text{ GeV}^2$ , and  $x_{Bj} = 0.25$ ; similar results are obtained in other kinematics.

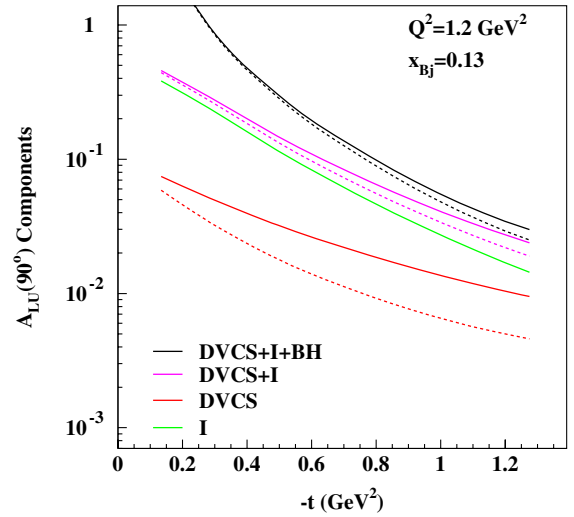


FIG. 14 (color online). Impact of different GPD components on data fit. The effect of including (solid curves) and excluding (dashed curves) the real part of the CFFs is shown for each component.  $Q^2 = 1.3 \text{ GeV}^2$ , and  $x_{Bj} = 0.12$ ; similar results are obtained in other kinematics.

relatively small contribution. To understand its impact on the various observables, in Fig. 14, we plotted results both including and excluding the real part.

Finally, in Fig. 15, we show the effect of the GPD  $\tilde{H}$  on the fit. We confirm the result also quantitatively reported in Ref. [17] that DVCS data from an unpolarized proton target at Jlab kinematics are dominated by the contribution of the GPD  $H$ . The dashed curves in the figure were obtained by disregarding the contribution of  $\tilde{H}$ .  $E$  and  $\tilde{E}$  have also very little impact on the data fit.

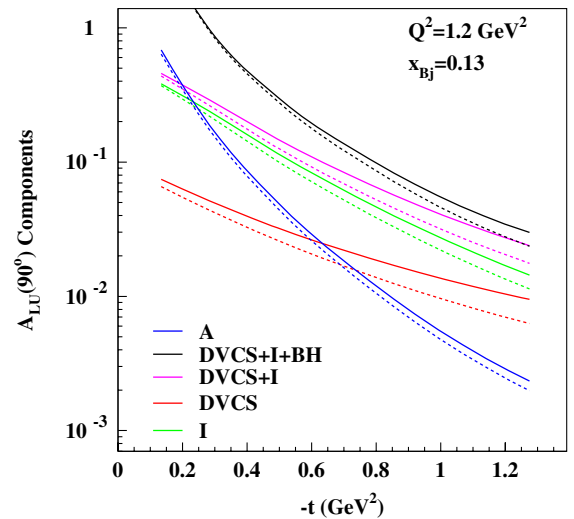


FIG. 15 (color online). Impact of different GPD components on data fit. The effect of including (solid curves) and excluding (dashed curves)  $\tilde{H}$  in the CFF evaluation is shown. The contribution of  $E$  is always negligible;  $Q^2 = 1.3 \text{ GeV}^2$ , and  $x_{Bj} = 0.12$ . Similar results are found in other kinematical bins.

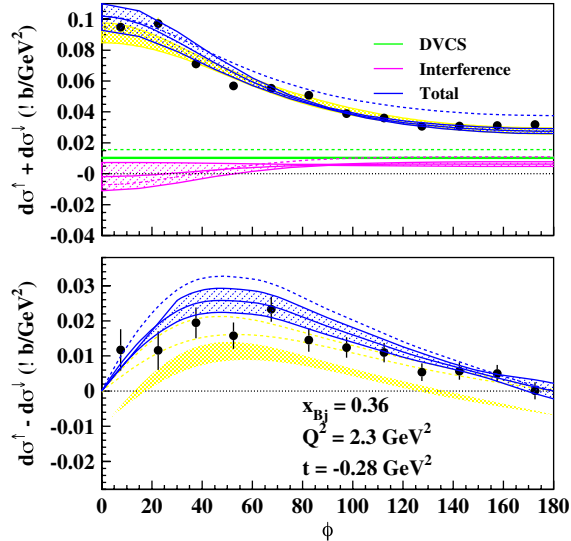


FIG. 16 (color online). Hall A data [49] for the “sum” (upper panel) and “difference” (lower panel) of the two electron beam polarizations. Shown are curves, including the contribution of the  $\zeta$ -dependent factor from Eq. (34) (solid lines) and neglecting it (dashed lines). All terms (DVCS, Interference, and Total) are shown for the sum graph. The wide yellow bands in both panels represent the error of the data fit. The green band in the asymmetry graph is the theoretical error from our parametrization.

In Fig. 16, we show the results of our fit vs Hall A data [49]. These are given as the “sum” and “difference” of the two polarizations for the electron beam. Together with the data, we also plot the results of a fit performed in [49] (wide yellow bands). All theoretical curves are shown with and without the  $\zeta$ -dependent correcting factor from Eq. (34). Moreover, while we confirm that the sum, or absolute cross section, part is dominated by the BH term,

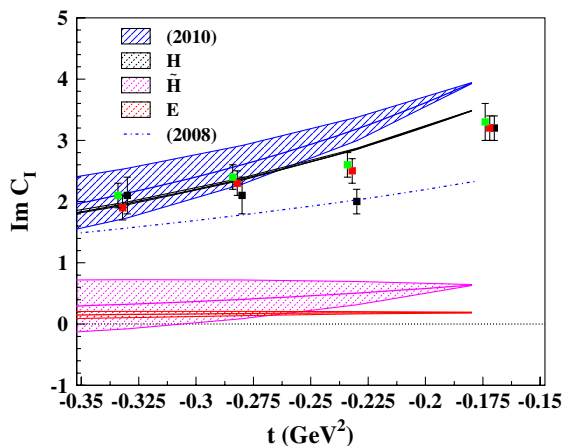


FIG. 17 (color online). Coefficient  $C$ , Eqs. (72), extracted from Hall A data [49]. Shown are the contributions from the GPDs,  $H$ ,  $\tilde{H}$ ,  $E$ , and  $\tilde{H}$ . All curves include the term in Eq. (34). A comparison with a previous prediction based on a simplified diquark model and, including  $H$ , only [25] is also shown.

we also point out the importance of the contribution from the pure DVCS scattering, or  $|T_{\text{DVCS}}|^2$ , at leading order in  $Q^2$ . Also shown are the theoretical error bands for the asymmetry. In Fig. 17, we compare our results to the experimental extraction of the imaginary part of the interference term coefficient in  $A_{LU}$ , Eqs. (81) and (85). The role of the CFF for  $\tilde{H}$  proves fundamental in determining the slope vs  $-t$  of this term. In order to illustrate this, we show a comparison with a previous calculation of the interference term where  $\tilde{H}$  was not included [25].

## 2. Hermes data

In the second phase of our analysis, we use our fit results to Jlab data to predict the quantities  $A_{LU}$ ,  $A_C$ , and  $A_{UT}$  extracted at Hermes [52,53]. Hermes data are provided as “coefficients” of the azimuthal angle-dependent terms. The dependence of these coefficients on the various kinematical variables is sensitive to the set of approximations that one uses in the extraction, thus affecting quantitative analyses. In order to facilitate the comparison and to once more show some of the subtleties involved, in Fig. 18, we show the results of our fit for  $A_{LU}$  vs  $-t$ ,  $Q^2$ , and  $x_{Bj}$ , respectively, calculated at each kinematical bin provided by Hermes [56] (curve denoted as “Hermes kinematics”) and at the nominal average values presented in each panel. It is interesting to notice that, due to the correlation between  $x_{Bj}$  and  $Q^2$  in the data, different features arise when using the average bin values. In the figure (lower panels),

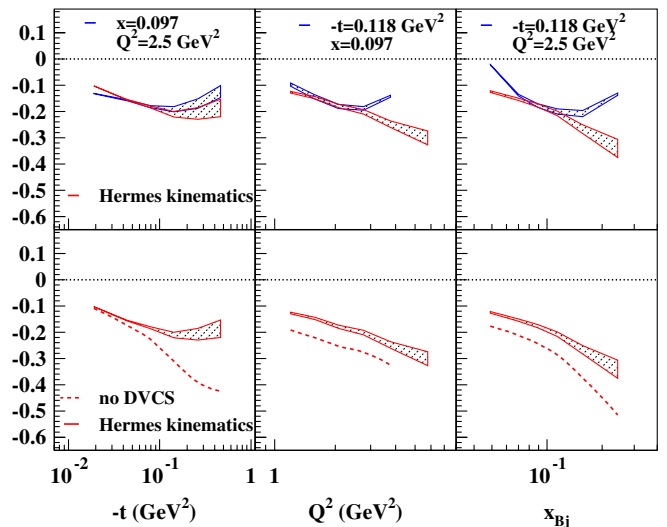


FIG. 18 (color online). Calculations at Hermes kinematics [52,53,56]. Shown is  $A_{LU}(90^\circ)$  vs  $-t$ ,  $Q^2$ , and  $x_{Bj}$ , respectively, calculated at each kinematical bin provided by Hermes [56] (curve denoted as “Hermes kinematics”) and at the nominal average values presented in each panel. It is interesting to notice that, due to the correlation between  $x_{Bj}$  and  $Q^2$  in the data, different features arise when using the average bin values. In the lower panels, we also show the effect of disregarding the DVCS term in the denominator (dashed curves).

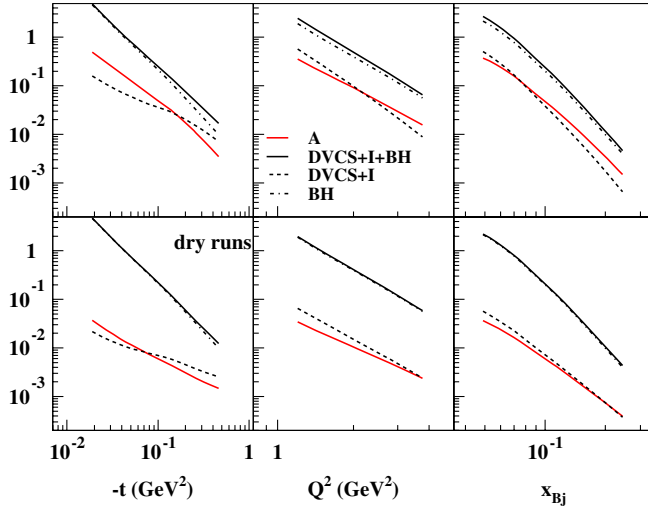


FIG. 19 (color online). Cross section components contributing to  $A_{LU}(90^\circ)$ :  $A$ , BH (dot-dashed lines), the sum of the  $T_{\text{DVCS}}^2$  and the BH/DVCS interference terms (dashed lines), and  $B$ , Eqs. (85). The curves in the figure were calculated for the same kinematical bins as in Fig. 18 [56]. In order to discern the role of the various components involving GPDs from the kinematics, we also show “dry runs” of our code in the lower panels obtained by setting all GPD factors equal to one.

we also show the effect of disregarding the DVCS term in the denominator. Similarly to the Jlab results, the GPD that the data are largely sensitive to is  $H$ , the role of the other GPDs being marginal. As a concluding remark on  $A_{LU}$ , we notice that Jefferson Lab Hall B data seem to suggest a

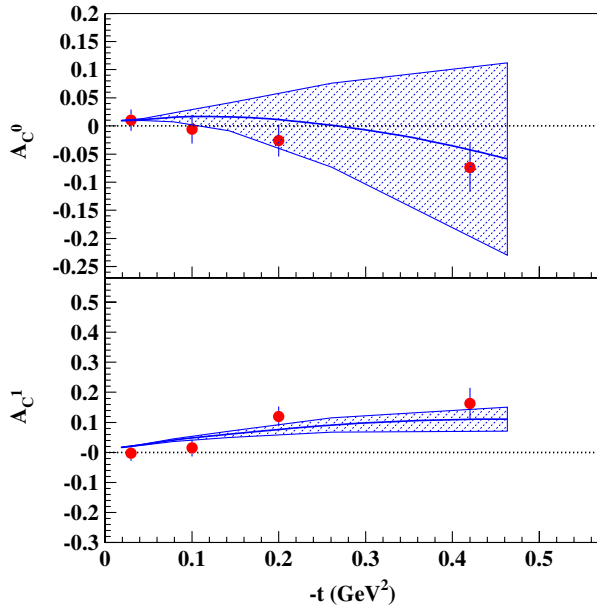


FIG. 20 (color online). Coefficients of the beam charge asymmetry,  $A_C$ , extracted from experiment [52,53]. The lower panel is the coefficient for the  $\cos\phi$ -dependent term in Eq. (82), while the upper panel is the  $\cos\phi$ -independent term.

decrease of  $A_{LU}$  with  $x_{Bj}$ . The curves in Fig. 18 used Jlab data in the fit and, therefore, they show a definite slope in  $x_{Bj}$ .

In Fig. 19, we show the different cross section components contributing to  $A_{LU}(90^\circ)$ , given by  $A$  and by the contributions from BH,  $T_{\text{DVCS}}^2$ , and the BH/DVCS interference terms in  $B$ , Eqs. (85). The curves in the figure were calculated for the same kinematical bins as in Fig. 18 [56]. In order to discern the role of the various components involving GPDs from the kinematics, we also show “dry runs” of our code in the lower panels obtained by setting all GPD factors equal to one. The various kinematical coefficients used in this analysis are written in Appendix D.

Finally, in Fig. 20 and 21, our predictions for  $A_C$  and  $A_{UT}$  are shown vs  $-t$ . The agreement with Hermes data is remarkably good within our theoretical error, despite the fact that we did not implement directly such data in the fit. Notice the larger error bar in  $A_C$  and  $A_{UT}^{\text{SI}}$ , which is dominated by the error on  $\tilde{H}$ , present in these observables. The notation we use in the figures, matching Eqs. (85) and Refs. [52,53,56], is

$$\begin{aligned} D(\phi)/(B(\phi) - D(\phi)) &\equiv A_C^0, \\ C(\phi)/(B(\phi) - D(\phi)) &\equiv A_C^1 \end{aligned}$$

(Fig. 20) and

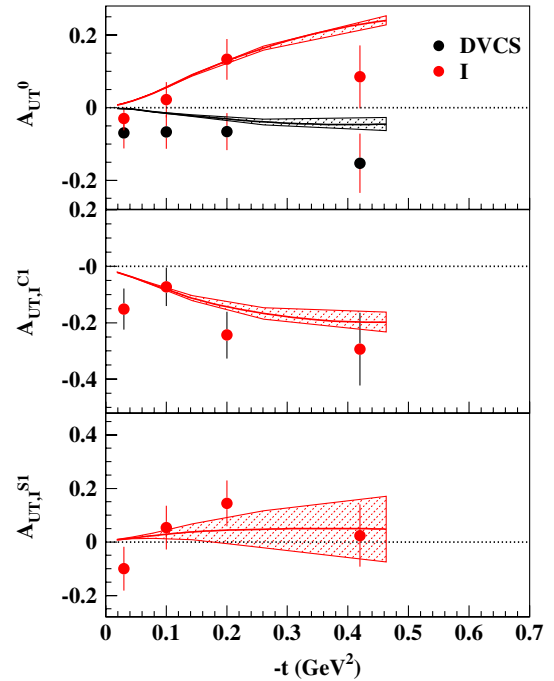


FIG. 21 (color online). Coefficients of the beam charge asymmetry,  $A_{UT}$ , extracted from experiment [52,53]. The upper panel shows the terms  $E$  and  $F$  from Eqs. (83) and (84), respectively; the middle panel shows  $G$ , and the lower panel  $H$ , both in Eq. (84). The curves are predictions obtained extending our quantitative fit of Jefferson Lab data to the Hermes set of observables.

$$\begin{aligned}
E(\phi)/(B(\phi) - D(\phi)) &\equiv A_{UT}^0(\text{DVCS}), \\
F(\phi)/(B(\phi) - D(\phi)) &\equiv A_{UT}^0(I), \\
G(\phi)/(B(\phi) - D(\phi)) &\equiv A_{UT,CI}^1, \\
H(\phi)/(B(\phi) - D(\phi)) &\equiv A_{UT,SI}^1
\end{aligned}$$

(Fig. 21).

## V. CONCLUSIONS AND OUTLOOK

In this paper, we have presented a parametrization of the chiral-even GPDs that is inspired by a physically motivated picture of the nucleon as a quark-diquark system with Regge behavior. The spin structure of each of the four GPDs is determined via the covariant quark-nucleon scattering amplitude, with a diquark exchange. The masses, couplings, and Regge power behavior that set the scale for the dependence on the kinematic variables,  $X$ ,  $\zeta$ ,  $t$ , and  $Q^2$ , are determined via a recursive procedure. We fit the parton distribution functions  $f_1$  and  $g_1$  for the  $u$  and  $d$  quarks with  $H(X, 0, 0)$  and  $\tilde{H}(X, 0, 0)$  at a low scale. The electromagnetic form factors,  $F_1(t)$  and  $F_2(t)$ , constrain the first  $X$  moments of  $H(X, \zeta, t)$  and  $E(X, \zeta, t)$ . These first moments are constrained to satisfy polynomiality, thereby removing the  $\zeta$  dependence and leaving only the  $t$  dependence. This requires fixing the parametrization of the ERBL region,  $X < \zeta$ , for all  $\zeta$  so as to satisfy a sum rule for the form factor. The same approach is used for the axial-vector form factor and  $\tilde{H}$ . Similarly, the pseudoscalar form factor constrains  $\tilde{E}$ , although we have not used that here (the contribution that is not dominated by the  $\pi$  pole is not well-known and is the subject of a forthcoming paper [32]).

In a previous paper, Goldstein and Liuti [19] have shown that the simple parton interpretation of the ERBL region is dubious, so the parametrization used here for that region is chosen to have a polynomial form and to satisfy the proper crossing symmetry while maintaining polynomiality for the first moments. This constrains the  $X - \zeta$  dependence through the sum rule, Eq. (51). Having fixed the parameters of the Regge and diquark functions (Table I), the set of measured DVCS observables can be determined using evolution equations to match the  $Q^2$  of different data sets. From these GPDs, the Compton form factors that enter the cross sections and asymmetries can be computed. Beam asymmetry data indicate the need for a damping of the higher  $\zeta$  behavior of the contributing CFFs. We incorporate this effect through a multiplicative function of  $X$ ,  $\zeta$ , and  $t$  that lowers the high  $\zeta$  value at higher  $t$  [Eq. (34)].

The final determination of the parameters provides an excellent fit to all of the available DVCS data. Newer DVCS cross section and asymmetry measurements at Jefferson Lab and COMPASS will provide a test of the flexibility of the model developed here. At this point, we see that this physically motivated model provides a far-reaching interpretation of the separate spin-dependent

GPDs, and thereby, a picture of the transverse structure of the nucleons will emerge.

A number of questions remain that are being addressed in ongoing work. The connection between the Regge-like behavior of these GPDs and the more general form of variable mass diquark exchanges has opened up the possibility of having the Regge behavior emerge from diquark mass variation. Such a variation will better approximate the Fock space structure of the nucleon. A second, important concern is the inclusion of sea quarks, whose contribution will affect the low  $x_{Bj}$  dependence, particularly the singlet, crossing even GPDs, whose Regge behavior is dominated by Pomeron exchange. Finally, the important extension of this parametrization scheme to the chiral-odd GPDs is critical for the phenomenology of deeply virtual meson electroproduction, which was begun particularly for the  $\pi^0$  in Ref. [21]. The connection of chiral-odd GPDs to the transversity structure of the nucleon is of great interest as a signal of quark and gluon orbital angular momentum.

## ACKNOWLEDGMENTS

We thank H. Moutarde for useful exchanges and for providing us with all available data sets. We are also indebted to Morgan Murray and Tanja Horn for comments and suggestions and to Saeed Ahmad for participating in the initial stages of this work. This work is supported by the U.S. Department of Energy Grants No. DE-FG02-01ER4120 (J. O. G. H., S. L.) and No. DE-FG02-92ER40702 (G. R. G.).

## APPENDIX A: USEFUL INTEGRATION FORMULAS

A crucial point regarding the  $\Delta_T$  dependence in Eqs. (27)–(30) is that the integral over  $\mathbf{k}_\perp$  can be done explicitly over the azimuthal angle first, to yield the angular dependence. This is clear in noting that  $k_1 + ik_2 = |\mathbf{k}_\perp|e^{i\phi}$  and  $\tilde{\mathbf{k}}_1 + i\tilde{\mathbf{k}}_2 = |\mathbf{k}_\perp|e^{i\phi} - (1 - X)/(1 - \zeta)\Delta_\perp$ , where  $\Delta_\perp$  can be chosen to be in the  $x$  direction with no loss of generality. Also,  $\Delta_\perp \cdot \mathbf{k}_\perp = \Delta_\perp |\mathbf{k}_\perp| \cos\phi$ . The  $\phi$  dependence comes only from the  $\mathbf{k}_\perp$  in the helicity flip numerators and the  $k'^2 = k^2 + \Delta^2 - k^+ \Delta^- + k^- \Delta^+ - 2\Delta_\perp \cdot \mathbf{k}_\perp$  in the denominators. When doing the integral over  $\phi$  from 0 to  $2\pi$ , the single factor  $e^{i\phi}$  gives 0, as does  $\cos\phi$  or  $\sin\phi$  alone. Hence, single flip amplitudes will begin at  $\Delta_\perp$  terms and double flip ones at  $\Delta_\perp^2$ . The integrals used are of the form

$$\int_0^{2\pi} \frac{1}{(a - b \cos\phi)^2} d\phi = \frac{2\pi a}{(a^2 - b^2)^{3/2}}, \quad (\text{A1a})$$

$$\int_0^{2\pi} \frac{\cos\phi}{(a - b \cos\phi)^2} d\phi = \frac{2\pi b}{(a^2 - b^2)^{3/2}}, \quad (\text{A1b})$$

where  $b = 2k_\perp \Delta_\perp$ , and  $a$  does not depend on  $\Delta_\perp$ .

### APPENDIX B: INITIAL SCALE GENERALIZED PARTON DISTRIBUTIONS

We present here a more practical version of the diquark contribution to the GPDs at the initial scale,  $Q^2 = 0.0936 \text{ GeV}^2$ . The complete parametrization needs to be multiplied by the Regge term provided in Eq. (34). By defining

$$L^2(X) = XM_X^2 + (1-X)M_\Lambda^2 - X(1-X)M^2, \quad (\text{B1a})$$

$$\mu = m + XM, \quad (\text{B1b})$$

$$\mu' = m + X'M, \quad (\text{B1c})$$

$$X' = \frac{X - \zeta}{1 - \zeta}, \quad (\text{B1d})$$

$$A = [L^2(X') + (1 - X')^2 \Delta_\perp^2]^2, \quad (\text{B1e})$$

$$B = 2[L^2(X') - (1 - X')^2 \Delta_\perp^2], \quad (\text{B1f})$$

all four GPDs can be written as follows:

$$F(X, \zeta, t) = \pi \mathcal{G}_1 (1-X)^{3/2} (1-X')^{3/2} \times \int_0^\infty \frac{d\kappa}{[\kappa + L^2(X)]^2} \frac{g_0 + g_1 \kappa + g_2 \kappa^2}{[A + B\kappa + \kappa^2]^{3/2}} + \mathcal{G}_2, \quad (\text{B2})$$

where  $\kappa \equiv k_T^2$ . One has for  $E$ ,

$$\mathcal{G}_1 = 2\mathcal{N}_E (1-X') \sqrt{1-\zeta} R(X, \zeta, t), \quad (\text{B3a})$$

$$\mathcal{G}_2 = 0, \quad (\text{B3b})$$

$$g_0 = \mu M [L^2(X') + (1 - X')^2 \Delta_\perp^2], \quad (\text{B3c})$$

$$g_1 = -M(\mu - 2\mu'), \quad (\text{B3d})$$

$$g_2 = 0. \quad (\text{B3e})$$

For  $\tilde{E}$ ,

$$\mathcal{G}_1 = 2\mathcal{N}_{\tilde{E}} (1-X') \sqrt{1-\zeta} \left(2 \frac{1-\zeta}{\zeta}\right) R(X, \zeta, t), \quad (\text{B4a})$$

$$\mathcal{G}_2 = 0, \quad (\text{B4b})$$

$$g_0 = \mu M [L^2(X') + (1 - X')^2 \Delta_\perp^2], \quad (\text{B4c})$$

$$g_1 = -M(\mu + 2\mu'), \quad (\text{B4d})$$

$$g_2 = 0. \quad (\text{B4e})$$

For  $H$ ,

$$\mathcal{G}_1 = \mathcal{N}_H \frac{1-\zeta}{\sqrt{1-\zeta}} R(X, \zeta, t), \quad (\text{B5a})$$

$$\mathcal{G}_2 = \frac{\zeta^2}{4(1-\zeta)} E, \quad (\text{B5b})$$

$$g_0 = \mu \mu' [L^2(X') + (1 - X')^2 \Delta_\perp^2], \quad (\text{B5c})$$

$$g_1 = \mu \mu' + [L^2(X') - (1 - X')^2 \Delta_\perp^2], \quad (\text{B5d})$$

$$g_2 = 1. \quad (\text{B5e})$$

For  $\tilde{H}$ ,

$$\mathcal{G}_1 = \mathcal{N}_{\tilde{H}} \frac{1-\zeta}{\sqrt{1-\zeta}} R(X, \zeta, t), \quad (\text{B6a})$$

$$\mathcal{G}_2 = \frac{\zeta^2}{4(1-\zeta)} \tilde{E}, \quad (\text{B6b})$$

$$g_0 = \mu \mu' [L^2(X') + (1 - X')^2 \Delta_\perp^2], \quad (\text{B6c})$$

$$g_1 = \mu \mu' - [L^2(X') - (1 - X')^2 \Delta_\perp^2], \quad (\text{B6d})$$

$$g_2 = -1. \quad (\text{B6e})$$

In the forward limit, the GPDs reduce to the form

$$G = \pi \mathcal{G}_1 (1-X)^3 \int_0^\infty d\kappa \frac{g_0 + g_1 \kappa + g_2 \kappa^2}{[\kappa + L^2(X)]^5}, \quad (\text{B7})$$

where the functions  $g_0$ ,  $g_1$ , and  $g_2$  are evaluated at  $\Delta_\perp^2 = 0$  and  $\zeta = 0$ . Solving the integral for each case, we get

$$H(X, 0, 0) = \pi (1-X)^3 \frac{2\mu^2 + L^2(X)}{6L^6} X^{-\alpha}, \quad (\text{B8})$$

$$\tilde{H}(X, 0, 0) = \pi (1-X)^3 \frac{2\mu^2 - L^2(X)}{6L^6} X^{-\alpha}, \quad (\text{B9})$$

$$E(X, 0, 0) = 2\pi (1-X)^4 \frac{\mu M}{3L^6} X^{-\alpha}, \quad (\text{B10})$$

$$\tilde{E}(X, 0, 0) = \pi M (1-X)^6 X^{-\alpha} \left[ \frac{M}{3L^6} \right. \quad (\text{B11})$$

$$\left. - \frac{4\mu[(1-2X)M^2 - M_X^2 + M_\Lambda^2]}{5L^8} \right]. \quad (\text{B12})$$

### APPENDIX C: PRINCIPAL VALUE INTEGRATION

The principal value integrations entering the CFFs defined in Eq. (3b) were carried out with the modified Gaussian method, yielding

$$\begin{aligned} \mathfrak{Re} \mathcal{H} &= \text{PV} \int_{\zeta/2}^1 dX \frac{H^+(X, \zeta, t)}{X - \zeta} + \int_{\zeta/2}^1 dX \frac{H^+(X, \zeta, t)}{X} \\ &= H(\zeta, \zeta, t) \ln \frac{1-\zeta}{\zeta/2} + \int_{\zeta/2}^1 dX \frac{H^+(X, \zeta, t) - H(\zeta, \zeta, t)}{X - \zeta} \\ &\quad + \int_{\zeta/2}^1 dX \frac{H^+(X, \zeta, t)}{X}. \end{aligned} \quad (\text{C1})$$

### APPENDIX D: KINEMATICAL COEFFICIENTS IN ASYMMETRIES AND CROSS SECTIONS

The kinematical coefficients in Eqs. (85) are

$$K_T^0(\phi) = \frac{-8K^2(2-y)^3}{1-y} \frac{1}{x_{Bj} y^3 P_1(\phi) P_2(\phi) t}, \quad (\text{D1})$$

$$K_T^1(\phi) = \frac{8K(2-y)}{x_{Bj} y^2 P_1(\phi) P_2(\phi) t}, \quad (\text{D2})$$

$$K_I^2(\phi) = \frac{-8K(2 - 2y + y^2)}{x_{Bj}y^3P_1(\phi)P_2(\phi)t}, \quad (\text{D3})$$

$$K_{\text{DVCS}}^0 = \frac{2(2 - 2y + y^2)}{(2 - x_{Bj})^2} \frac{1}{y^2Q^2}, \quad (\text{D4})$$

$$K_{\text{DVCS}}^{UT} = K \sqrt{\frac{Q^2}{(1 - y)M^2}} (2 - 2y + y^2) \frac{4}{2 - x_{Bj}} \frac{1}{y^2Q^2}, \quad (\text{D5})$$

$$K_I^{UT} = -8 \frac{M}{Q^2} \frac{2 - 2y + y^2}{2 - x_{Bj}} \sqrt{1 - y}, \quad (\text{D6})$$

with [10]

$$P_1(\phi) = -\frac{1}{y\sqrt{1 + \epsilon^2}} (H + 2K \cos\phi), \quad (\text{D7})$$

$$P_2(\phi) = \left(1 + \frac{t}{Q^2}\right) - P_1(\phi), \quad (\text{D8})$$

where

$$H = \left(1 - y - \frac{1}{2}y\epsilon^2\right) \left(1 + \frac{t}{Q^2}\right) - (1 - x_{Bj})(2 - y) \frac{t}{Q^2}.$$

- 
- [1] F. Sabatie, J. Roche, A. Camsonne, and C. Munoz Camacho, <http://hallaweb.jlab.org/experiment/DVCS/>; L. Elouadrhiri, <http://www.jlab.org/Hall-B/clas12/>.
- [2] F. Kunne and A. Bressan, “COMPASS Status Report 2011,” CERN Report No. CERN-SPSC-2011-024, 2011; G. Mallot, “COMPASS Status Report 2010,” CERN Report No. CERN-SPSC-2010-018, 2010.
- [3] H. Gallagher and D. Harris, in *Neutrino-Nucleus Interactions in the Few-GeV Region*, edited by G.P. Zeller, J.G. Morfin, and F. Cavanna, AIP Conf. Proc. No. 967 (AIP, New York, 2007), p. 158.
- [4] D. Muller, D. Robaschik, B. Geyer, F.M. Dittes, and J. Horejsi, *Fortschr. Phys.* **42**, 101 (1994).
- [5] X.D. Ji, *Phys. Rev. D* **55**, 7114 (1997).
- [6] A. V. Radyushkin, *Phys. Rev. D* **56**, 5524 (1997).
- [7] J. C. Collins, L. Frankfurt, and M. Strikman, *Phys. Rev. D* **56**, 2982 (1997).
- [8] J. C. Collins, T. C. Rogers, and A. M. Stasto, *Phys. Rev. D* **77**, 085009 (2008).
- [9] M. Burkardt, *Int. J. Mod. Phys. A* **18**, 173 (2003); *Phys. Rev. D* **62**, 071503 (2000); **66**, 119903(E) (2002).
- [10] A. V. Belitsky, D. Mueller, and A. Kirchner, *Nucl. Phys. B* **629**, 323 (2002).
- [11] G. R. Goldstein, and S. Liuti, *Phys. Rev. D* **80**, 071501 (2009).
- [12] I. V. Anikin and O. V. Teryaev, *Phys. Rev. D* **76**, 056007 (2007).
- [13] M. Diehl and D. Yu Ivanov, *Eur. Phys. J. C* **52**, 919 (2007).
- [14] K. Kumericki and D. Mueller, *Nucl. Phys. B* **841**, 1 (2010).
- [15] K. Kumericki, D. Mueller, and K. Passek-Kumericki, *Nucl. Phys. B* **794**, 244 (2008).
- [16] M. Guidal and H. Moutarde, *Eur. Phys. J. A* **42**, 71 (2009).
- [17] H. Moutarde, *Phys. Rev. D* **79**, 094021 (2009); [arXiv:1010.4521](https://arxiv.org/abs/1010.4521).
- [18] M. V. Polyakov and K. M. Semenov-Tian-Shansky, *Eur. Phys. J. A* **40**, 181 (2009), and references therein.
- [19] G. R. Goldstein and S. Liuti, [arXiv:1006.0213](https://arxiv.org/abs/1006.0213).
- [20] M. Diehl, *Phys. Rep.* **388**, 41 (2003).
- [21] S. Ahmad, G. R. Goldstein, and S. Liuti, *Phys. Rev. D* **79**, 054014 (2009).
- [22] S. J. Brodsky, F. E. Close, and J. F. Gunion, *Phys. Rev. D* **8**, 3678 (1973).
- [23] S. J. Brodsky and F. J. Llanes-Estrada, *Eur. Phys. J. C* **46**, 751 (2006); S. J. Brodsky, F. J. Llanes-Estrada, and A. P. Szczepaniak, *Phys. Rev. D* **79**, 033012 (2009).
- [24] S. Ahmad, H. Honkanen, S. Liuti *et al.*, *Eur. Phys. J. C* **63**, 407 (2009).
- [25] S. Ahmad, H. Honkanen, S. Liuti *et al.*, *Phys. Rev. D* **75**, 094003 (2007).
- [26] R. Jakob, P. J. Mulders, and J. Rodrigues, *Nucl. Phys. A* **626**, 937 (1997).
- [27] L. P. Gamberg, G. R. Goldstein, and M. Schlegel, *Phys. Rev. D* **77**, 094016 (2008).
- [28] M. Burkardt, *Int. J. Mod. Phys. A* **18**, 173 (2003), and references therein.
- [29] S. Liuti and S. K. Taneja, *Phys. Rev. D* **70**, 074019 (2004).
- [30] M. Diehl, *Eur. Phys. J. C* **25**, 223 (2002).
- [31] J. Kuti and V. F. Weisskopf, *Phys. Rev. D* **4**, 3418 (1971).
- [32] G. Goldstein, J. G. Gonzalez, and S. Liuti (unpublished).
- [33] K. Goeke, M. V. Polyakov, and M. Vanderhaeghen, *Prog. Part. Nucl. Phys.* **47**, 401 (2001).
- [34] S. Alekhin, K. Melnikov, and F. Petriello, *Phys. Rev. D* **74**, 054033 (2006).
- [35] P. M. Nadolsky, H.-L. Lai, Q.-H. Cao *et al.*, *Phys. Rev. D* **78**, 013004 (2008).
- [36] A. D. Martin, W. J. Stirling, R. S. Thorne *et al.*, *Eur. Phys. J. C* **63**, 189 (2009).
- [37] A. V. Vinnikov, [arXiv:hep-ph/0604248](https://arxiv.org/abs/hep-ph/0604248).
- [38] Y. Goto *et al.* (Asymmetry Analysis Collaboration), *Phys. Rev. D* **62**, 034017 (2000).
- [39] E. Leader, A. V. Sidorov, and D. B. Stamenov, *Phys. Rev. D* **73**, 034023 (2006).
- [40] J. J. Kelly, *Phys. Rev. C* **70**, 068202 (2004).
- [41] A. J. R. Puckett, E. J. Brash, M. K. Jones *et al.*, *Phys. Rev. Lett.* **104**, 242301 (2010).
- [42] M. R. Schindler and S. Scherer, *Eur. Phys. J. A* **32**, 429 (2007).

- [43] T. Gorringer and H.W. Fearing, *Rev. Mod. Phys.* **76**, 31 (2003).
- [44] R. Bradford, A. Bodek, H. S. Budd *et al.*, *Nucl. Phys. B, Proc. Suppl.* **159**, 127 (2006).
- [45] X.-D. Ji and R. F. Lebed, *Phys. Rev. D* **63**, 076005 (2001).
- [46] P. Hagler *et al.* (LHPC Collaboration), *Phys. Rev. D* **77**, 094502 (2008).
- [47] R.D. Ball, L. Del Debbio, S. Forte *et al.*, *Nucl. Phys.* **B838**, 136 (2010).
- [48] H. Honkanen, S. Liuti, J. Carnahan *et al.*, *Phys. Rev. D* **79**, 034022 (2009).
- [49] C. Munoz Camacho *et al.* (Jefferson Lab Hall A and Hall A DVCS Collaborations), *Phys. Rev. Lett.* **97**, 262002 (2006).
- [50] M. Mazouz *et al.* (Jefferson Lab Hall A Collaboration), *Phys. Rev. Lett.* **99**, 242501 (2007).
- [51] F.X. Girod *et al.* (CLAS Collaboration), *Phys. Rev. Lett.* **100**, 162002 (2008).
- [52] A. Airapetian *et al.* (HERMES Collaboration), *J. High Energy Phys.* 06 (2008) 066.
- [53] A. Airapetian *et al.* (HERMES Collaboration), *J. High Energy Phys.* 11 (2009) 083.
- [54] P. Kroll, M. Schurmann, and P.A.M. Guichon, *Nucl. Phys.* **A598**, 435 (1996).
- [55] P.A.M. Guichon, G.Q. Liu, and A.W. Thomas, *Nucl. Phys.* **A591**, 606 (1995).
- [56] M. Murray (private communication).